https://doi.org/10.5194/egusphere-2025-6127
Preprint. Discussion started: 11 January 2026

HyperGas 1.0: A Python package for analyzing hyperspectral data for greenhouse gases from retrieval to emission rate quantification

Xin Zhang[1], Joannes D. Maasakkers[1], Tobias A. de Jong[1], Paul Tol[1], Frances Reuland[2], Adam R. Brandt[2], Eric A. Kort[3], Taylor J. Adams[3], and Ilse Aben[1,4]

[1]SRON Space Research Organisation Netherlands, Leiden, 2333 CA, The Netherlands
[2]Department of Energy Science & Engineering, Stanford University, Stanford, California 94305, United States
[3]Department of Climate & Space Sciences & Engineering, University of Michigan, Ann Arbor, MI 48109, USA
[4]Department of Earth Sciences, Vrije Universiteit Amsterdam, Amsterdam, 1081 HV, The Netherlands

Correspondence: Xin Zhang (xin.zhang@sron.nl)

Abstract.

We present *HyperGas*, an open-source Python package for the retrieval and estimation of atmospheric greenhouse gas concentration enhancements and plume emission rates using data from hyperspectral imagers such as the PRecursore IperSpettrale della Missione Applicativa (PRISMA), the Environmental Mapping and Analysis Program (EnMAP), and the Earth Surface Mineral Dust Source Investigation (EMIT). The software is designed for compatibility with any three-dimensional hyperspectral radiance dataset. *HyperGas* supports multiple retrieval algorithms, including matched filter and lognormal matched filter, and offers two emission rate estimation methods: the integrated mass enhancement and cross-sectional flux approaches. The software provides a scalable batch-processing framework that supports data workflows from radiances to emission rates and an interactive graphical user interface that enables visualization of gas plumes. Built on high-level data structures such as xarray and CSV, *HyperGas* simplifies metadata handling and facilitates robust analysis and visualization. The package provides a robust foundation for community use and expansion. This toolkit aims to advance atmospheric monitoring capabilities and support both research and operational applications of greenhouse gas monitoring.

1 Introduction

Greenhouse gases such as carbon dioxide (CO_2) and methane are the primary drivers of anthropogenic climate change, contributing to global warming and altering the Earth's energy balance (Intergovernmental Panel on Climate Change (IPCC), 2023). Monitoring these gases at facility-scale is increasingly important for identifying emission sources, supporting and verifying mitigation efforts, and informing climate policy. Spaceborne hyperspectral imagers (HSI), with their ability to capture hundreds of narrow, contiguous spectral bands, have been demonstrated to enable the detection and quantification of large methane and CO_2 emission plumes from individual facilities (Guanter et al., 2021; Jacob et al., 2022; Cusworth et al., 2023; Thorpe et al., 2023; Borger et al., 2025; Zhang et al., 2025). However, as no operational greenhouse gas products exist for these missions, such analyses have so far been limited to a few specialized research groups. Furthermore, the analysis requires several

https://doi.org/10.5194/egusphere-2025-6127
Preprint. Discussion started: 11 January 2026

steps that can diverge between different analysis groups. To broaden access and facilitate wider scientific use, we introduce an open-source framework for greenhouse gas analysis from HSI data.

Hyperspectral imagers have become a powerful tool for a wide range of remote sensing applications (Qian, 2021). HSIs were originally designed to characterize Earth's surface features such as mineral distributions. They have high spatial and spectral resolution that also enables the detection of greenhouse gases, most notably CO_2 and methane, under favorable conditions (Thorpe et al., 2023). Their fine spectral resolution (∼10 nm) allows for more accurate detection and quantification of atmospheric greenhouse gases compared to multispectral imaging (∼100 nm; e.g., Sentinel-2 and Landsat) but is still limited compared to area mappers such as Global Observing SATellite (GOSAT) and TROPOspheric Monitoring Instrument (TROPOMI) that allow the precise estimation of background gas concentrations (e.g., Jacob et al., 2022). Over the past two decades, advancements in imaging spectrometer technologies have led to a surge in the availability and quality of spaceborne HSI data. From early missions like Earth Observing-1 (EO-1)/Hyperion (Pearlman et al., 2001) to newer platforms such as GaoFen-5 (Liu et al., 2019), the PRecursore IperSpettrale della Missione Applicativa (PRISMA; Loizzo et al., 2018; Cogliati et al., 2021), the Environmental Mapping and Analysis Programme (EnMAP; Guanter et al., 2015; Storch et al., 2023), the Earth Surface Mineral Dust Source Investigation (EMIT; Green et al., 2020, 2023), and the Carbon Mapper Coalition satellites (Tanager-series; Duren et al., 2025), there has been a steady improvement in spatial, spectral, and temporal resolutions. These instruments have been applied to detect methane and CO_2 emitters around the world (Guanter et al., 2021; Thorpe et al., 2023; Han et al., 2024; Zhang et al., 2025). With upcoming missions like the Copernicus Hyperspectral Imaging Mission for the Environment (CHIME; Rast et al., 2021) and the Surface Biology and Geology mission (SBG; Cawse-Nicholson et al., 2021), researchers and analysts will soon have access to an unprecedented volume of high-resolution hyperspectral data.

Existing open-source tools, such as mag1c (https://github.com/markusfoote/mag1c/) and emit-ghg (https://github.com/emit-sds/emit-ghg), are restricted to a single HSI or data format. To overcome these limitations, we introduce *HyperGas*, an open-source Python package designed to streamline the analysis of greenhouse gases from different HSI data. *HyperGas* provides modular tools and default settings to guide users through each stage of the analysis pipeline, from gas concentration enhancement retrieval to emission quantification, using an optimized and extendable architecture that facilitates additions from the user community. The package supports both automated batch processing and interactive exploration through a graphical user interface, enabling flexibility across a wide range of use cases and expertise levels. For advanced users, *HyperGas* offers a high degree of customization, allowing for the integration of novel algorithms and processing strategies. In this paper, we present the design principles behind *HyperGas*, demonstrate its capabilities through a number of real-world case studies involving methane and CO_2, and outline how it can serve as a foundation for reproducible, scalable greenhouse gas analysis using HSI data.

2 Software description

We have designed the *HyperGas* package for Level 1 (L1, radiance) to Level 4 (L4, e.g., emission rate estimates) products, including the following steps described in Sect. 2.1–2.4 (Figure 1):

1. Data preparation (L1; Section 2.1)

https://doi.org/10.5194/egusphere-2025-6127
Preprint. Discussion started: 11 January 2026

2. Greenhouse gas retrieval (L2; Section 2.2)
3. Plume detection and segmentation (Defined here as L3; Section 2.3)
4. Emission estimation (L4; Section 2.4)

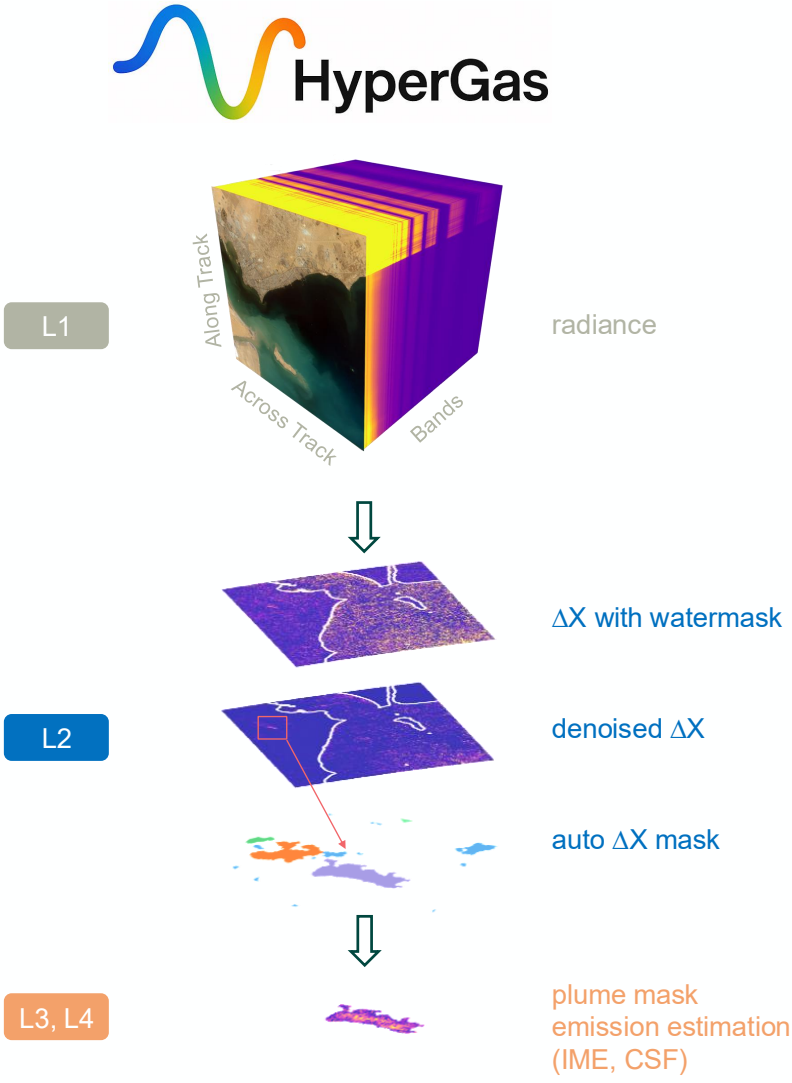

Figure 1. Workflow of the *HyperGas* package (L1–L4). The input consists of L1 calibrated radiance at sensor sampling. Greenhouse gas retrieval produces L2 concentration enhancements (ΔX), which are automatically denoised for plume detection and masking. The plume data (L3) is then used to estimate emissions (L4) with the integrated mass enhancement (IME) and cross-sectional flux (CSF) methods.

We describe the user interface in Section 2.5. The *HyperGas* framework supports a wide range of hyperspectral satellite data and aircraft observations, as long as they contain radiance data for retrieving greenhouse gases. For existing L2 data, the

https://doi.org/10.5194/egusphere-2025-6127
Preprint. Discussion started: 11 January 2026

package can also be employed to only perform plume detection, segmentation, and emission estimation. Several additional data inputs are used in HyperGas. Due to the significant differences in surface albedo and thereby radiance levels over land and water (Funk et al., 2001; Foote et al., 2020), the retrieval process incorporates a water mask to separately process land and water pixels, as described in Sections 2.1.2 and 2.2. Additionally, wind reanalysis data (Section 2.1.3) are essential for estimating greenhouse gas emission rates from plume imagery, as outlined in Section 2.4.

2.1 Data preparation

2.1.1 L1 radiance data

HyperGas v1.0 initially focuses on processing L1 radiance data from three HSIs (PRISMA, EnMAP, and EMIT) but can be expanded for other hyperspectral data products such as aircraft observations. These three instruments cover key absorption bands of methane (weak and strong absorption windows around 1700 and 2300 nm) and CO_2 (1928–2200 nm) within their relevant spectral ranges, enabling targeted gas detection (Foote et al., 2021). Table 1 provides a summary of key characteristics of the hyperspectral satellite instruments.

Table 1. Description of hyperspectral satellite instruments.

Instrument	Launch date	Nadir pixel size	Coverage	Spectral resolution *	Overpass time
EnMAP	2022-04-01	30 m	30×30 km^2	∼7.4 nm	Sun-Synchronous Low Earth Orbit with an equator crossing times of 11:00
EMIT	2022-07-14	60 m	80 km width	∼7.4 nm	ISS orbit with variable overpass time
PRISMA	2019-03-22	30 m	30×30 km^2	∼10 nm	Sun-Synchronous Low Earth Orbit with an equator crossing times of 10:30

*Typical average spectral resolution in the shortwave infrared (SWIR) range.

For PRISMA, the L1 data are obtained from the PRISMA Portal (https://prisma.asi.it/); for EnMAP, these come from the EOWEB GeoPortal (https://eoweb.dlr.de/); and for EMIT, users can download L1 data from NASA Earthdata (https://search.earthdata.nasa.gov/). No pre-treatment is applied to the L1 data. Because HSI file formats vary across different products, we have integrated multiple HSI readers into another Python package named *Satpy* (Raspaud et al., 2025), ensuring a standardized data-loading interface of the three-dimensional `xarray.DataArray (bands, y, x)` format (Hoyer and Hamman, 2017). This makes it easy to support new HSI data.

PRISMA Level 1 data lacks geolocation details, such as rational polynomial coefficients (RPCs) or a geometric lookup table (LUT), which are typically used for precise image positioning, or georeferencing. Therefore, we manually correct the offset for L2–L4 products using Ground Control Points (GCPs) that are visually identified from distinct features on Earth's surface (e.g., road intersections), while RPCs and LUTs are applied for EnMAP and EMIT data, respectively.

https://doi.org/10.5194/egusphere-2025-6127
Preprint. Discussion started: 11 January 2026

2.1.2 Water mask

We classify pixels as land or water by using 10-m integrated data from both OpenStreetMap (OSM) and ESA WorldCover databases (Kennedy et al., 2024). ESA WorldCover data primarily encompass Canada, Alaska, and Russia, while OpenStreetMap data covers the remaining global regions. Both datasets are combined to create a global dataset. The implemented water mask identifies both coastal waters and major inland water bodies.

HyperGas also supports two other datasets available through the cartopy feature interface (https://cartopy.readthedocs.io/stable/matplotlib/feature_interface.html): the Global Self-consistent, Hierarchical, High-resolution Geography (GSHHG) database and the 10-m Natural Earth dataset. The water mask is used in the clustering of pixels to separately apply a retrieval for land and water pixels (Section 2.2.1). Figure 2 compares the water masks around the Caspian Sea as well as a K-means clustering approach that further disaggregates the scene (Section 2.2.1). The OSM and ESA WorldCover datasets effectively differentiate between land and water, whereas the GSHHG dataset misclassifies some sea areas as land, and the Natural Earth dataset omits inland water bodies. These differences in masking can lead to variations in retrieval results (see Sect. 2.2.1).

2.1.3 Wind data

Wind speed and direction control greenhouse gas transport in the atmosphere, thus they are important input data for plume determination and emission quantification. The default wind product used in the analysis is the European Centre for Medium-Range Weather Forecasts Reanalysis 5 (ERA5, 0.25° × 0.25°) 10-m hourly wind data (Hersbach et al., 2020; Carver and Merose, 2023). The GEOS Forward Processing (GEOS-FP, 0.25° latitude × 0.3125° longitude) 10-m wind data is also supported.

2.2 Greenhouse gas retrieval

2.2.1 Matched filter

To determine the amount of gas (e.g., methane or CO_2) above the background in the atmospheric column at a specific location, we apply a mathematical method known as the linear matched filter. This approach has been successfully applied to satellite and aircraft observations (Thompson et al., 2015; Foote et al., 2021; Thorpe et al., 2023; Roger et al., 2024). By default, we exclude water bands (1358–1453 nm and 1814–1961 nm) which can affect the retrieval of methane and CO_2. The modeled spectrum affected by the gas absorption ($\boldsymbol{x_m}$) is defined according to the Beer-Lambert law:

$$\boldsymbol{x_m} = \boldsymbol{x_r} e^{-\boldsymbol{k}\Delta X} \tag{1}$$

where $\boldsymbol{x_r}$ is the reference spectrum and $\boldsymbol{k}$ is a unit absorption spectrum. The strong absorption windows of 2100–2450 nm for methane and 1930–2200 nm for CO_2 are selected for calculating the gas column enhancement (ΔX). The matched filter method treats the background spectral signature as a Gaussian distribution ($\mathcal{N}$) with a mean vector $\boldsymbol{\mu}$ and covariance matrix $\boldsymbol{\Sigma}$.

https://doi.org/10.5194/egusphere-2025-6127
Preprint. Discussion started: 11 January 2026

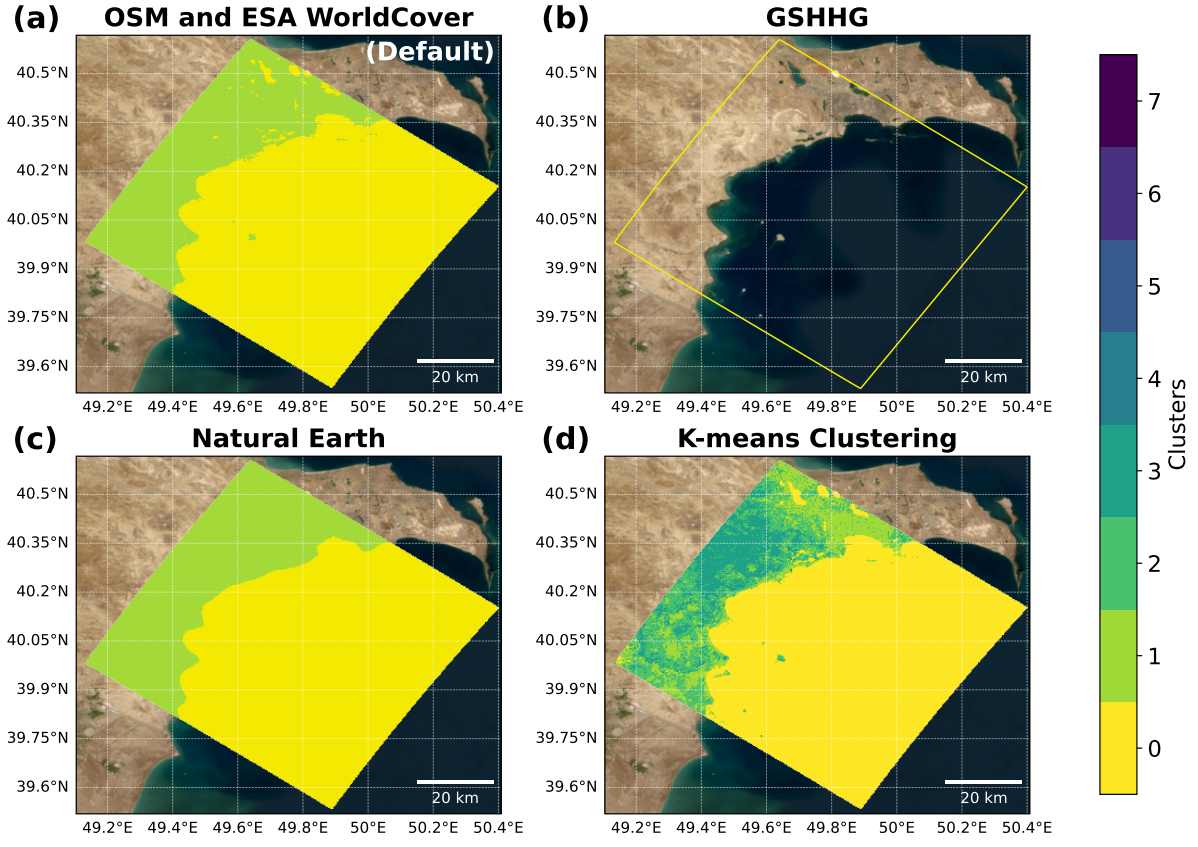

Figure 2. EMIT pixel clusters derived from (a) OpenStreetMap (OSM) and ESA WorldCover databases, (b) the Global Self-consistent, Hierarchical, High-resolution Geography database (GSHHG), (c) the Natural Earth dataset, and (d) k-means clustering. Water pixels are assigned a value of zero (yellow), while land pixels are assigned values greater than or equal to one, with specific classifications determined using the k-means clustering method. In the case of the GSHHG dataset, all pixels are classified as land but are shown as transparent with the EMIT scene outlined in yellow for comparison against the ESRI World Imagery. Source: Esri | Powered by Esri.

The radiance spectrum (L) considers two scenarios: a null hypothesis H_0 representing background conditions, and an alternative hypothesis H_1 indicating the presence of enhanced gas concentrations (Thompson et al., 2015).

$$H_0 : L \sim \mathcal{N}(\boldsymbol{\mu}, \boldsymbol{\Sigma}); H_1 : L \sim \mathcal{N}(\boldsymbol{\mu} + \Delta X \boldsymbol{t}, \boldsymbol{\Sigma}) \quad (2)$$

The target signature $\boldsymbol{t}$ is defined as the product of the background mean radiance ($\boldsymbol{\mu}$) and the negative gas absorption coefficient ($\boldsymbol{k}$). To derive $\boldsymbol{k}$, we apply a radiative transfer model (Gloudemans et al., 2008), incorporating the instrument's spectral response function characterized by its central wavelength and FWHM (Thompson et al., 2015). The atmosphere is divided into vertical layers with a thickness of 1 km up to an altitude of 25 km, 2.5 km between 25 and 50 km, and 5 km above 50 km altitude. We use the seasonal Air Force Geophysical Laboratory (AFGL) atmospheric constituent profiles and simulate

https://doi.org/10.5194/egusphere-2025-6127
Preprint. Discussion started: 11 January 2026

various gas enhancement scenarios in the lowermost atmospheric layer (0–1 km) using the forward model. For methane, we evaluate enhancements from 0 to 6400 ppb in geometric progression (doubling from 100 ppb), while CO_2 enhancements range from 0 to 160 ppm (doubling from 2.5 ppm), reflecting the broader dynamic range and higher background concentration of CO_2 compared to methane. The $\boldsymbol{k}$ value for each band is determined through linear regression between the natural logarithm of the simulated radiance and gas enhancement values. The optimal estimate of the enhancement factor ΔX is obtained through maximum likelihood estimation:

$$\Delta X = \frac{(\boldsymbol{t}-\boldsymbol{\mu})^T \boldsymbol{\Sigma}^{-1} (\boldsymbol{L}-\boldsymbol{\mu})}{(\boldsymbol{t}-\boldsymbol{\mu})^T \boldsymbol{\Sigma}^{-1} (\boldsymbol{t}-\boldsymbol{\mu})} \tag{3}$$

Optical aberrations can cause variations in central wavelength and spectral resolution among detectors within the same array (Guanter et al., 2009), leading to non-uniformity across data-cube columns in the across-track direction. Therefore, the matched filter is implemented separately for each along-track column. We apply the matched filter to each cluster (Fig. 2) separately to account for differences in background signals (e.g., land versus water pixels). The algorithm is applied through the *Spectral Python (SPy, https://github.com/spectralpython/spectral)* package, which supports the matched filter method. Figure 3 shows the retrieved methane enhancements (ΔXCH_4) associated with methane leaks in Azerbaijan, derived using different water masks. The GSHHG mask, which treats all pixels as land, produces overestimated methane retrievals with higher noise levels (Fig. 3b). Results obtained with Natural Earth data are similar to those from the default OSM and ESA WorldCover masks, though Natural Earth fails to effectively differentiate inland/coastal water pixels (Fig. 3c).

Previous studies on aircraft observations suggest that applying the matched filter to clustered pixels can reduce background noise such as the albedo effect caused by roads and building infrastructures (Funk et al., 2001; Thorpe et al., 2013). We first apply the principal component analysis (PCA) to reduce the dimension of the data space. Then we use the k-means algorithm to classify all pixels into clusters. Users can adjust the `kmeans.nclusters` argument to test the sensitivity (Funk et al., 2001). The k-means clustering approach tends to underestimate methane enhancements, presumably due to the reduced pixel count allocated to each cluster (Fig. 3d). We have also tested the cluster-tuned matched filter in urban areas (Appendix Figure A1), however, the results are still noisy, making it challenging to differentiate plumes from the background. The improved retrieval performance of previous airborne imaging spectrometers is likely related to their higher spatial resolution (3–8 m) and narrower swath width (∼5 km) compared with HSIs, which also leads to longer observed plumes within a single scene. Therefore, *HyperGas* does not rely on the k-means method but instead applies land and water masks derived from the OSM and ESA WorldCover datasets.

2.2.2 Lognormal matched filter

One limitation of the matched filter is the linear approximation, which could lead to underestimated enhancements in large plumes (Schaum, 2021; Pei et al., 2023). Therefore, *HyperGas* provides the lognormal matched filter method which applies logarithms to both sides of Eq. (1):

https://doi.org/10.5194/egusphere-2025-6127
Preprint. Discussion started: 11 January 2026

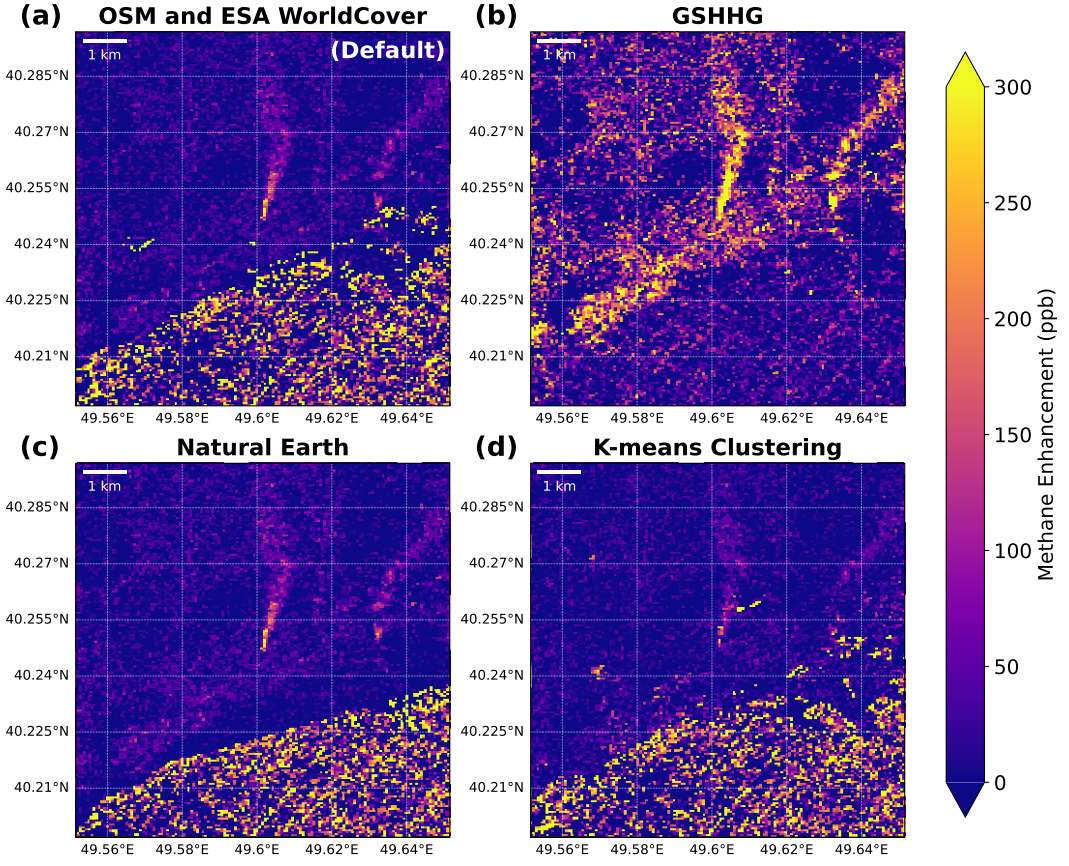

Figure 3. Retrieved methane enhancements from the EMIT observation over Azerbaijan on April 21, 2024, based on matched filter analysis applied to each pixel cluster as defined in Fig. 2.

$$\ln(\boldsymbol{x_m}) = \ln(\boldsymbol{x_r}) - \boldsymbol{k}\Delta X \tag{4}$$

This addresses the limitation of the first-order Taylor expansion, which assumes weak absorption that can be approximated as linear, whereas in regions of strong methane enhancement the absorption departs from this linear behavior. Then the optimal estimate of ΔX is derived as below:

$$\Delta X = \frac{(\boldsymbol{k}-\tilde{\boldsymbol{\mu}})^T \tilde{\boldsymbol{\Sigma}}^{-1}(\tilde{\boldsymbol{L}}-\tilde{\boldsymbol{\mu}})}{(\boldsymbol{k}-\tilde{\boldsymbol{\mu}})^T \tilde{\boldsymbol{\Sigma}}^{-1}(\boldsymbol{k}-\tilde{\boldsymbol{\mu}})} \tag{5}$$

where $\tilde{\boldsymbol{\mu}}$ is the mean log background radiance, $\tilde{\boldsymbol{\Sigma}}$ is the covariance matrix of the log background radiance, and $\tilde{\boldsymbol{L}}$ is the log radiance spectrum. Figure 4 compares the results obtained using the matched filter and the lognormal matched filter. The

https://doi.org/10.5194/egusphere-2025-6127
Preprint. Discussion started: 11 January 2026

methane enhancement differences can reach up to 50 ppb, potentially impacting subsequent emission rate quantification. Since the lognormal matched filter only supports positive radiances and may increase background noise, *HyperGas* defaults to the matched filter and uses the lognormal matched filter for large methane emissions (e.g., > 10 t h^{-1} as discussed in Pei et al. (2023)). Because the CO_2 data are noisier than the methane data, *HyperGas* does not automatically switch to the lognormal matched filter for CO_2.

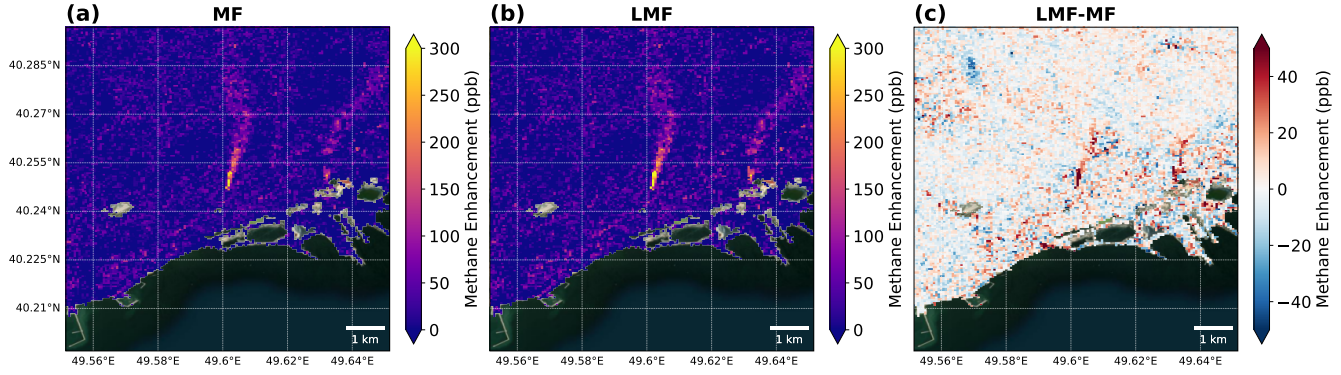

Figure 4. Retrieved methane enhancements from the EMIT observation over Azerbaijan on April 21, 2024, using (a) the matched filter method and (b) the lognormal matched filter method. Panel (c) shows the difference between the two retrievals. Water pixels are masked using the OSM and ESA WorldCover data sets. Background imagery source: Esri | Powered by Esri.

2.3 Plume detection

For plume detection, we perform the matched filter over the entire near-infrared window (1300–2500 nm, Roger et al., 2024), instead of only over the strong methane (2100–2450 nm) and CO_2 (1928–2200 nm) absorption windows, to mitigate the background noise in (for example) urban areas. This includes the additional methane absorption features around 1700 nm as well as additional background wavelengths without sensitivity to methane. Then, we apply a Chambolle total variation (TV) denoising filter (Chambolle, 2004) to reduce noise and obtain a smoother ΔX field. This technique reduces noise by minimizing the total variation of the image, which refers to the integral of the gradient magnitude, while preserving sharp features such as edges. Unlike traditional smoothing methods such as median filtering, TV denoising effectively suppresses noise while preserving meaningful structures, making it more suitable for retaining localized methane enhancements. Because different scenes detected by different instruments have different noise levels, we calibrate the denoisers for each scene and instrument using J-Invariance (Batson and Royer, 2019). The denoised ΔX field is only used for generating plume masks because of its differing magnitude, while the emission rate calculation relies on ΔX data retrieved from strong absorption windows without denoising. Figure 5a shows an example of the denoised ΔXCH_4 field for the scene from Fig. 3a.

We derive gas plume masks using a semi-supervised method that starts by applying a watershed technique to the denoised fields (Fig. 5b) with the *tobac* Python package. This method has been applied to track convective clouds (Heikenfeld et al.,

https://doi.org/10.5194/egusphere-2025-6127
Preprint. Discussion started: 11 January 2026

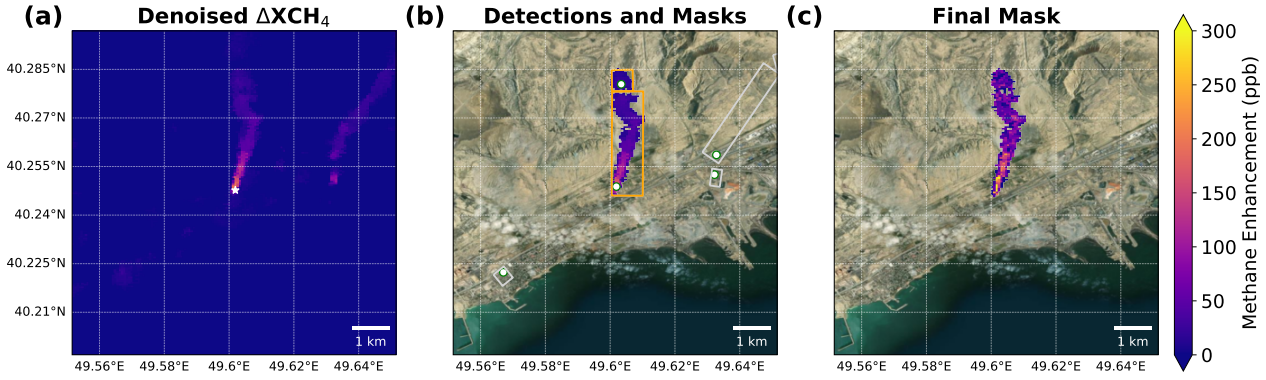

Figure 5. Plume mask creation process for one of the plumes from Fig. 3a. (a) The denoised Methane enhancement (ΔXCH_4) field obtained by applying the Chambolle total variance denoising (TV) filter to ΔXCH_4 within the 1300∼2500 nm window. The white star is the identified source location for the western plume. (b) The initial plume masks derived from the watershed algorithm for the western plume. White dots indicate high-ΔXCH_4 locations, while rectangles represent the minimum rotated rectangles for each mask. Orange rectangles denote masks with azimuth differences less than 30°, and gray rectangles correspond to other potential plumes. (c) The final ΔXCH_4 plume mask. Background imagery source: Esri | Powered by Esri.

2019), NO_2 plumes in TROPOMI observations (Zhang et al., 2023), and methane plumes in hyperspectral observations (Zhang et al., 2025). It treats pixel values as a topographic surface and separates them into different basins. We use a threshold of two standard deviations about the mean to identify localized high-enhancement features. We then use a threshold of three standard deviations to further separate features that were connected using the lower threshold (Fig. 5b; Rast et al., 2021). Once features are determined, the watershed expands outward from the features until it reaches the lower threshold (2nd standard deviation). We dilate these masks by 180 m and merge overlapping masks. Emission sources are manually identified based on wind data and ESRI imagery, the mask containing the emission source is then used as the source's plume mask. Figure 5c demonstrates the mask determined for one of the identified methane emission plumes in the scene. To ensure plumes originate from the same source, we limit the azimuth difference of the oriented envelope (minimum rotated rectangle) to less than 30° relative to that of the first plume mask containing the source (e.g., orange rectangles in Fig. 5b), assuming minimal wind direction changes near the source. If a plume is truncated as a result, *HyperGas* allows users to increase the dilation and azimuth difference to obtain a more appropriate plume mask (e.g., the eastern plume in Fig. 5a). Non-detects are classified when no plume mask is detected near the source of interest. Users can inspect the masked plumes through the graphical user interface (Sect. 2.5.2) to evaluate correlation with additional data fields such as albedo and RGB imagery to ensure the identified plume is not an artifact (e.g., smoke).

2.4 Emission estimation

Since the matched filter assumes plume signals are sparse (i.e., present in only a small fraction of pixels), we exclude pixels within identified plume masks when computing $\boldsymbol{\mu}$ and $\boldsymbol{\Sigma}$, so that background statistics are estimated only from non-plume

https://doi.org/10.5194/egusphere-2025-6127
Preprint. Discussion started: 11 January 2026

pixels and the sparsity assumption remains valid. The retrieval is then rerun to generate the final emission rate products. This two-step reprocessing approach reduces bias in background radiance estimates and typically yields higher methane emission rates.

Two widely used methods for estimating source emission rates from plume observations are the integrated mass enhancement (IME) method (Varon et al., 2018), which relates the total plume mass enhancement to the emission rate through a wind-speed-dependent parameterization, and the cross-sectional flux (CSF) method (Varon et al., 2018; Kuhlmann et al., 2024), which estimates the source rate as the product of methane enhancement and wind speed integrated across the plume width perpendicular to the wind direction. Both methods are available in *HyperGas* and described below, including the calibration of the required effective wind speed.

2.4.1 Estimation methods

We apply the IME method as the default method to estimate gas emission rates (Q in kg h^{-1}):

$$Q = \frac{\mathrm{IME} \cdot U_{\mathrm{eff,IME}}}{L} \tag{6}$$

where IME is the total gas mass enhancement (kg) within the plume mask, L (m) is the square root of the plume area, and $U_{\mathrm{eff,IME}}$ is the effective wind speed (m/s). The total gas mass enhancement is calculated by summing the product of the column mass enhancement ($\Delta\Omega$, kg m^{-2}) and the area of each pixel (m^2). The column mass enhancement $\Delta\Omega$ is derived from ΔX:

$$\Delta\Omega = \frac{M_X}{M_a}\Omega_a \Delta X \tag{7}$$

where M$_X$ and M$_a$ are the molar masses (kg mol^{-1}) of gas X and dry air (28.96×10^{-3} kg mol^{-1}), and Ω_a is the column of dry air (kg m^{-2}). Ω_a is defined as the ratio of surface pressure, obtained from GEOS-FP or ERA5 reanalysis data, to the acceleration of gravity.

In addition to the IME method using the full plume mask, *HyperGas* supports IME estimates with maximum fetch limits (IME-limit), which are particularly useful for characterizing elongated plumes (Duren et al., 2019; Thorpe et al., 2023; CarbonMapper, 2025).

Another method to calculate the emission rate is the CSF method. This method is especially useful if gaps in the detected plume, for example, caused by low albedo, make the estimate based on the total IME less reliable. Here, the source rate is estimated as the product of the cross-plume gas enhancement integral and a different effective wind speed ($U_{\mathrm{eff,CSF}}$):

$$Q = U_{\mathrm{eff,CSF}} \int_a^b \Delta\Omega(x,y)\, dy \tag{8}$$

Here, the x-axis aligns with the wind direction, while the y-axis is oriented perpendicular to it. The integral is evaluated between the plume boundaries [a, b], as defined by the cross section in the plume mask. The centerline is defined by fitting

https://doi.org/10.5194/egusphere-2025-6127
Preprint. Discussion started: 11 January 2026

a weighted cubic polynomial through the plume enhancement field, where weights correspond to gas enhancements. Fitting is performed in a coordinate system rotated to align with the principal plume direction (source to enhancement-weighted centroid), with ridge regularization (α = 0.1) to ensure smooth solutions. This plume-aligned cubic fit improves the quadratic method in *ddeq* (Kuhlmann et al., 2024) by better capturing plume curvature. Cross-sectional lines are positioned at equal arc-length intervals along the centerline. Each line is oriented perpendicular to the local centerline tangent where it intersects the plume mask. The spacing between CSF sections is set to 2.5×pixel resolution, rather than 1×pixel resolution, to reduce overlap between adjacent sections and ensure sufficient independence of sampled data.

2.4.2 Wind calibrations

For both the IME and CSF, an effective wind speed is required, which needs to be related to the model's wind speed parameters. To calibrate $U_{\mathrm{eff,IME}}$ and $U_{\mathrm{eff,CSF}}$ against the domain-averaged 10 m wind speeds (U_{10}), we have used five 3-hour large-eddy simulations (LES) performed using the Weather Research and Forecasting model (WRF-LES) at 25 m spatial resolution and 30 s temporal resolution (Varon et al., 2018; Maasakkers et al., 2022). For EnMAP and PRISMA, which have a spatial resolution of $\sim$ 30 m, we use the original 25 m data. For EMIT, which has a coarser resolution of $\sim$ 60 m, the data are resampled to 50 m. Simulations are conducted for two source types: a point source (e.g., oil and gas leaks or underground coal mine ventilation shafts; Sadavarte et al., 2021) and a 275 $\times$ 275 m^2 area source (e.g., landfills; Maasakkers et al., 2022). Emission rates are randomly scaled from 1–30 t h^{-1} for methane (Zhang et al., 2025) and 0.5–30 kt h^{-1} for CO_2 (Cusworth et al., 2023). The first simulation hour is used for turbulence spin-up, and the last two hours are used in the wind calibration.

To incorporate realistic backgrounds, we overlay LES plumes onto cropped measured L2 scenes free of detected gas plumes for each imager. Backgrounds are drawn from three representative surface types: bright and homogeneous (Xinjiang, China), bright and heterogeneous (Anna Creek, Australia), and dark and heterogeneous (Madrid, Spain). For each simulated plume, $U_{\mathrm{eff,IME}}$ is computed as QL/IME, where Q is known, and L/IME is calculated from the plume mask. Despite differences in background complexity, the denoising step enables robust plume detection (Fig. 6d–f), and calibration coefficients are consistent across scenes (Fig. 6g–i). We therefore combine all 3600 cases to derive final calibration parameters for methane and CO_2 (Table 2 and 3).

We evaluate the mean magnitude of U_{10} from three LES-derived wind products for the wind calibration: at-site, in-plume, and 6×6 km^2 domain-averaged. At-site wind calibration is suitable for controlled releases with co-located wind measurements (Sherwin et al., 2023, 2024), whereas in-plume and domain-averaged products are better suited for applications relying on reanalysis wind speed data. Figure 6g–i shows that calibration results are similar across the three wind products. Accordingly, *HyperGas* defaults to the domain-averaged calibration for typical use cases involving reanalysis winds. While *HyperGas* allows users to input custom wind speeds, they must adjust the calibration settings in the configuration file to match their inputs if those products have different characteristics than the ones used here.

https://doi.org/10.5194/egusphere-2025-6127
Preprint. Discussion started: 11 January 2026

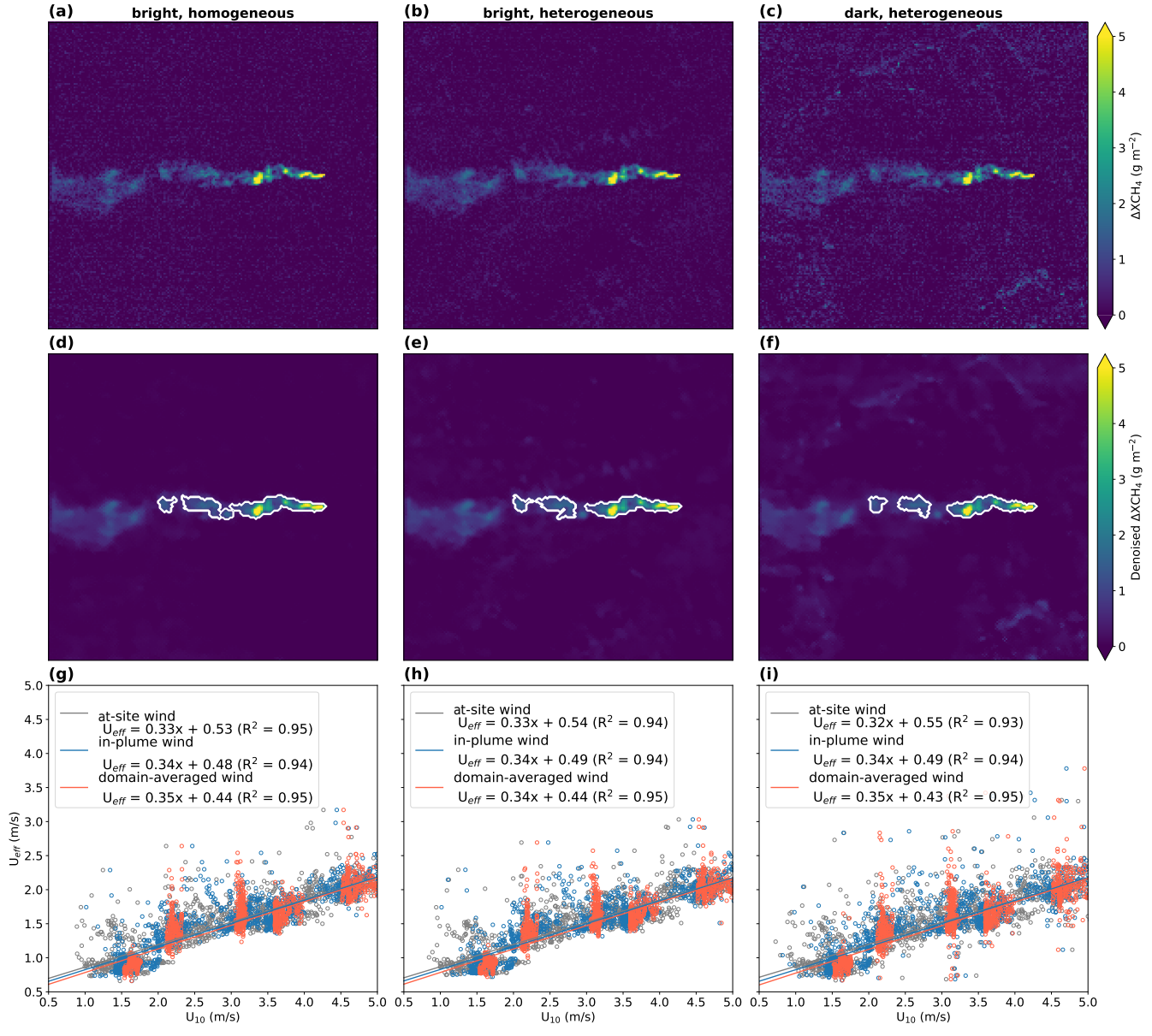

Figure 6. (a–c) Methane enhancement fields from point-source large eddy simulations over three EMIT scenes: bright and homogeneous, bright and heterogeneous, and dark and heterogeneous. (d–f) Corresponding denoised methane fields for the scenes shown in (a–c), with plume mask outlines shown in white. (g–i) Wind calibration results using three wind speed samplings: at-site values, in-plume estimates, and domain-averaged values.

https://doi.org/10.5194/egusphere-2025-6127
Preprint. Discussion started: 11 January 2026

Table 2. Wind calibration settings used by default in the IME and CSF methods for methane, based on domain-averaged wind fields.

Method	Instrument	Source Type	Slope	Intercept	R^2
IME	EMIT	point	0.35	0.43	0.95
	EnMAP	point	0.32	0.45	0.95
	PRISMA	point	0.31	0.43	0.93
	EMIT	area	0.39	0.63	0.89
	EnMAP	area	0.37	0.68	0.85
	PRISMA	area	0.37	0.69	0.77
CSF	EMIT	point	1.12	0.00	0.91
	EnMAP	point	1.15	0.00	0.90
	PRISMA	point	1.13	0.00	0.88
	EMIT	area	1.22	0.00	0.89
	EnMAP	area	1.30	0.00	0.87
	PRISMA	area	1.29	0.00	0.84

Table 3. Similar to Table 2 but for CO_2.

Method	Instrument	Source Type	Slope	Intercept	R^2
IME	EMIT	point	0.34	0.44	0.94
	EnMAP	point	0.31	0.46	0.94
	PRISMA	point	0.32	0.44	0.94
CSF	EMIT	point	1.10	0.00	0.90
	EnMAP	point	1.15	0.00	0.90
	PRISMA	point	1.13	0.00	0.88

2.4.3 Emission uncertainty quantification

Our estimation of emission uncertainty for both the IME and CSF method accounts for three sources of uncertainty: wind speed error, retrieval random error, and wind calibration uncertainty (Varon et al., 2019, 2020; Maasakkers et al., 2022). Wind speed error is quantified by applying a relative error of 50% for wind speeds below 3 m/s and a fixed error of 1.5 m s^{-1} for wind speeds exceeding 3 m/s (Varon et al., 2018; Zhang et al., 2025). To evaluate retrieval random error, we apply the same plume mask shape to non-plume areas across the scene, avoiding any overlap with the original plume location, and then calculate the standard deviation of the resulting emission rates (Varon et al., 2019; Zhang et al., 2025). Wind calibration error is the final source of uncertainty in our estimation. For point sources, the average U_{eff} fit residual is incorporated by adding it to the fitted U_{eff} equation, so that the fitting's typical deviation is propagated into the uncertainty calculation. The area-source calibration method assumes a uniform methane emission distribution over a 275 $\times$ 275 m^2 region, even though actual emission patterns

https://doi.org/10.5194/egusphere-2025-6127
Preprint. Discussion started: 11 January 2026

may be more complex (Maasakkers et al., 2022). To evaluate the uncertainty associated with this assumption, we apply the point-source calibration instead and examine the resulting variations in emission rates. The total uncertainty is defined as the square root of the sum of the squares of the individual uncertainties.

2.4.4 Plume fetch limits and controlled releases

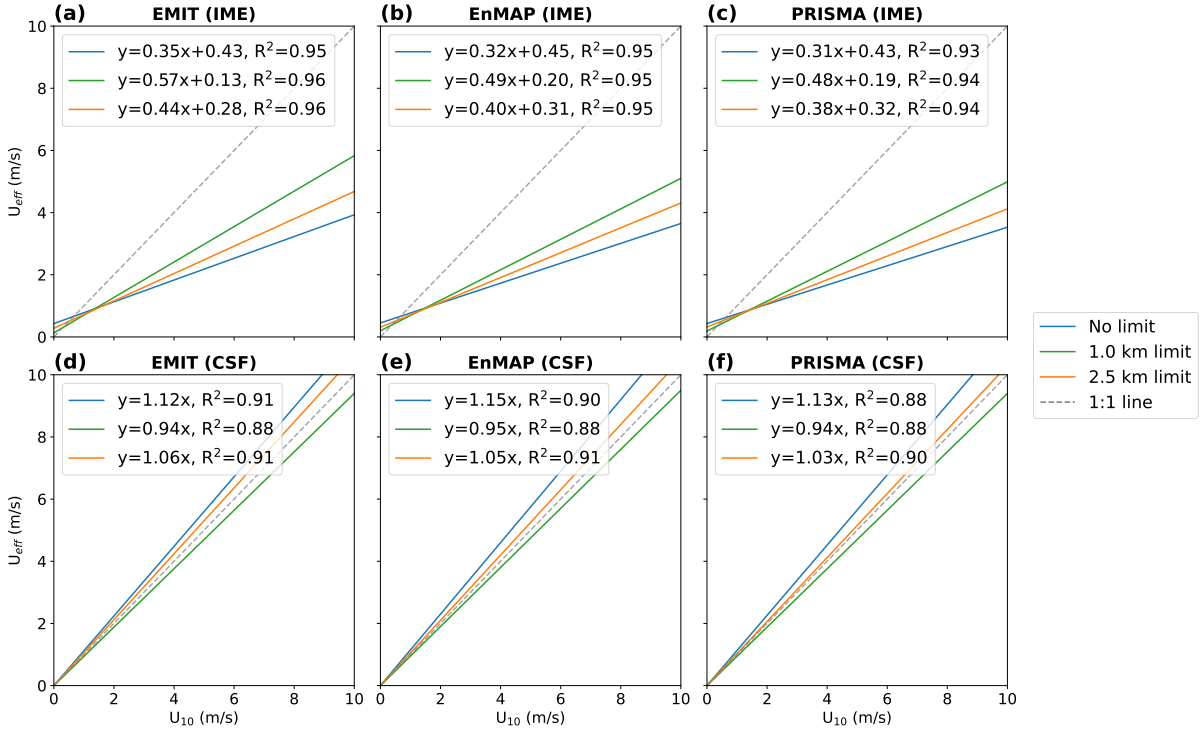

Figure 7. (a–c) Point-source IME calibrations for EMIT, EnMAP, and PRISMA. Colors indicate different fetch limits. (d–f) Same as (a–c), but using the CSF method.

Figure 7 shows wind calibrations for the IME and CSF methods across different plume length limits. Since Carbon Mapper applies a 2.5 km fetch limit (CarbonMapper, 2025), We have performed a sensitivity test using two thresholds: 1 km and 2.5 km (as used by for example Carbon Mapper). The IME method with a 1 km plume limit has a significantly higher calibration slope compared to other configurations (Fig. 7a–c). The response of calibration slopes to decreasing fetch limits differs between the IME and CSF methods (Fig. 7d–f). This divergence reflects fundamental differences in methodology: restricting the fetch limit to 1 km reduces the number of plume pixels available for integration in the IME method, resulting in lower emission estimates when the shortened plume length cannot compensate for the reduced total gas mass enhancement. Conversely, the CSF method, which relies on cross-sectional measurements, may not sample broadly enough to produce a representative emission rate. Then, we split the final two hours of simulation data into calibration and validation subsets to assess whether applying fetch limits

https://doi.org/10.5194/egusphere-2025-6127
Preprint. Discussion started: 11 January 2026

would improve performance during validation. However, the slopes between the true emission rates and the calibrated estimates remained approximately 1 across all fetch limits, indicating no improvement.

We also validated our default IME estimates using 19 Stanford controlled releases conducted in 2024 and 2025 (Reuland et al., 2025; Reuland and Brandt, 2025). Because all plume lengths were under 1 km, which could be short for reliable CSF estimation, we do not perform CSF validation for these data. This also means any differences between the IME and IME fetch estimates are purely caused by different wind calibration coefficients and not by different sampling of the plumes. Figure 8 shows that the results do not differ significantly across the various fetch limits. *HyperGas* currently defaults to wind calibration without any fetch limitation. In the future, controlled release experiments involving elongated plumes may support IME calibration in two key ways: (1) evaluating the accuracy of different fetch limits, and (2) enabling wind calibration directly using measured U_{10} data, which can then be applied to other cases with available wind observations.

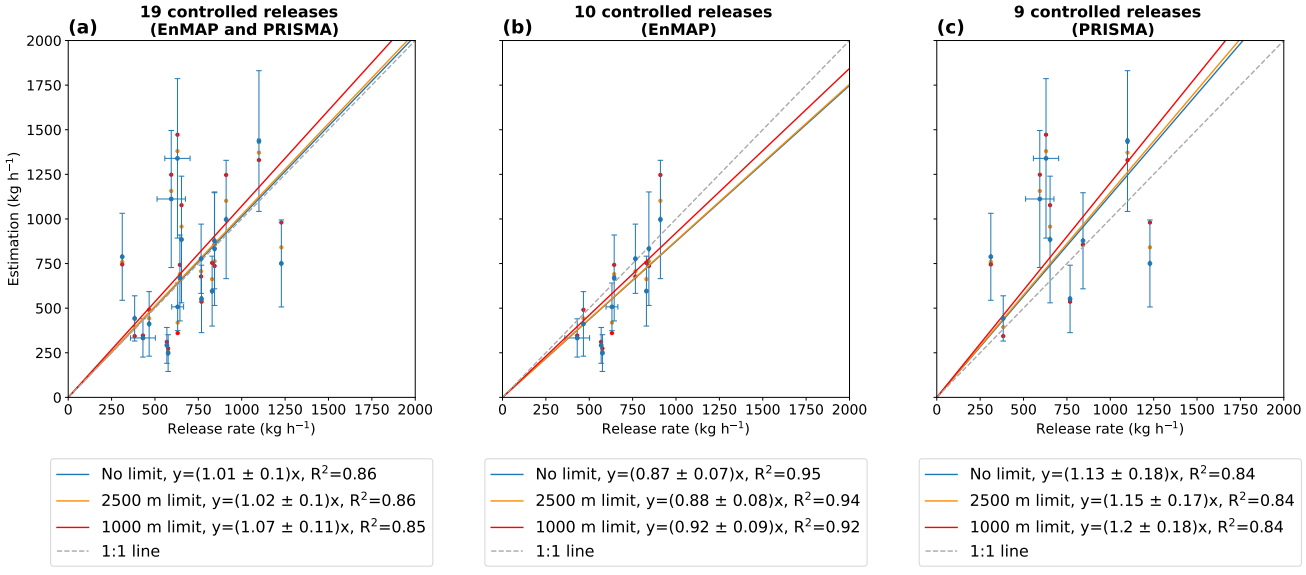

Figure 8. Quantification performance of methane-emission estimates using the IME method under different fetch limits (none, 2500 m, and 1000 m) with calibrations shown in Fig. 7a–c. (a) Controlled releases observed by both EnMAP and PRISMA. (b) EnMAP only. (c) PRISMA only. Regression lines are fitted with Ordinary Least Squares (OLS). Estimation errors are derived from *HyperGas* outputs. The release-rate errors are estimated as the standard deviation of mean emission rates released over consecutive time windows starting 1-5 minutes before and ending at the overpass time (i.e., [T–1 min, T], [T–2 min, T], . . . , [T–5 min, T]). For clarity, scatter points for the fetch-limited results are shown without error bars.

2.5 User interface

In addition to accessing functions via the Python API, *HyperGas* users can use Python batch processing scripts and an interactive application to efficiently process data from L1 to L4.

https://doi.org/10.5194/egusphere-2025-6127
Preprint. Discussion started: 11 January 2026

2.5.1 Batch processing

The general data processing workflow is outlined below:

- `l2b_process.py` and `l2b_plot.py`: Generate L2 products, visualizations, and a summary HTML file that lets users compare different scenes by toggling layers.
- `App`: Add plume markers interactively using the graphical user interface (see Sect. 2.5.2).
- `l3b_process.py`: Produce L3 and L4 products, figures, and HTML files. This step can also be performed within the app.
- (optional) `l2b_reprocess.py` and `l3b_reprocess.py`: Rerun the retrieval and emission rate estimates by excluding the plume pixels from each column of observations.

The variables included in the L2–L3 products are listed in Appendix Table B1. The L4 CSV file contains key plume-level information, including location, overpass time, wind conditions sampled from reanalysis products at the source location, emission rate and associated uncertainty, IME/CSF metrics, and additional details (For a full description, see the *HyperGas* User Guide: https://hypergas.readthedocs.io/).

2.5.2 Interactive app

The emission rate calculation process begins with identifying plume source locations using HTML files generated by the script `l2b_plot.py`. This script embeds multiple L2B figures into a single HTML file, including key visualizations such as albedo, raw and denoised gas retrievals, plume masks, and wind vectors. By default, the interface displays only the denoised gas field for each observation group, allowing direct comparison of plume characteristics, especially changes in plume direction due to wind across different observation days. Users can then interactively add plume markers through a Streamlit-based web application that dynamically renders HTML content and executes embedded Python code. Because plume source locations may differ between observations, users must place markers individually for each L2B file. The selected marker positions are saved in the GeoJSON format to ensure accurate spatial referencing.

Once all marker files are ready, the `l3b_process.py` script automatically generates plume-level NetCDF files and computes emission rates for all cases. For a more streamlined and case-specific workflow, users can use the "Emission" page of the application, which provides a customizable interface for entering relevant parameters, such as site name, sector, wind speed, and surface pressure. Upon submission, the app generates a comprehensive output, displaying the final plume visualization and a corresponding L4 summary table on the same page (Fig. 9).

3 Applications

HyperGas currently supports the detection, retrieval, and quantification of methane and CO_2 plume emissions across various sectors. In the following sections, we present several examples of methane and CO_2 plumes observed in different contexts.

https://doi.org/10.5194/egusphere-2025-6127
Preprint. Discussion started: 11 January 2026

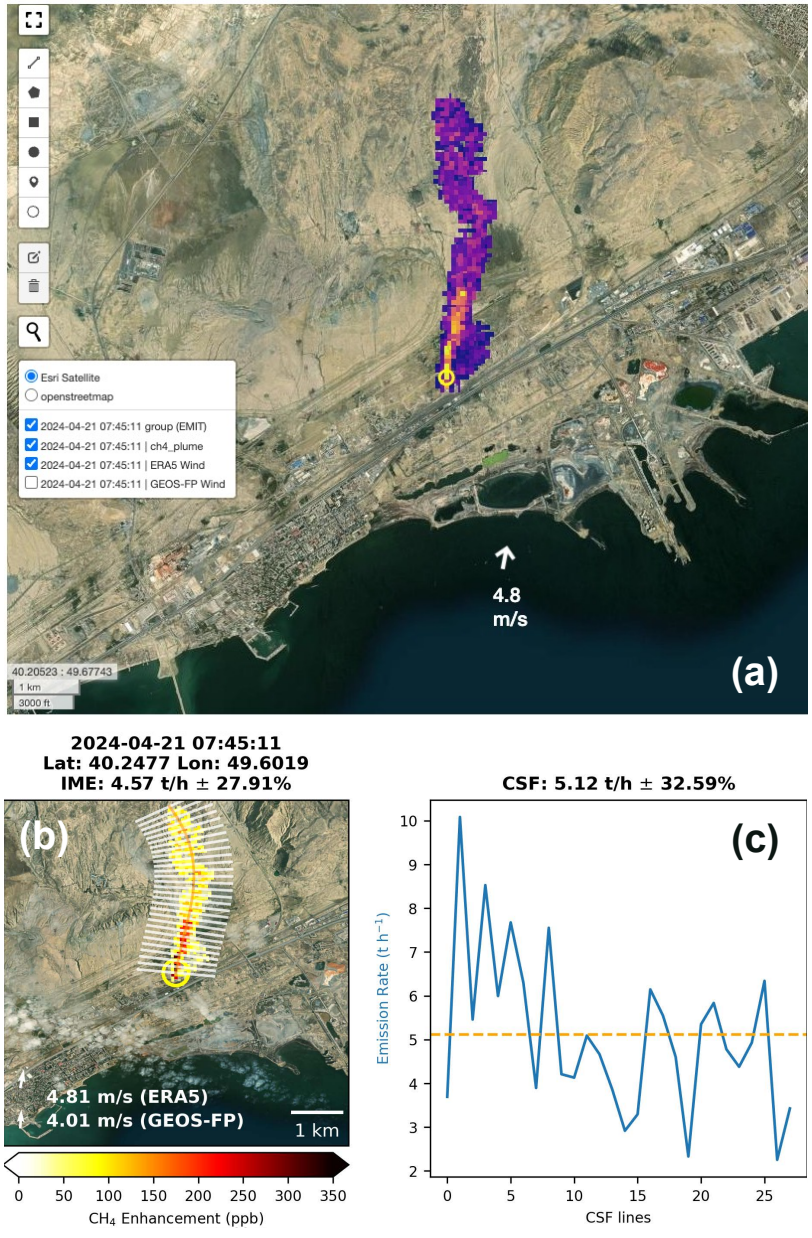

Figure 9. Example overview from the interactive application. (a) Methane plume overlaid on an ESRI basemap. Source: Esri | Powered by Esri. The emission source is marked with a yellow circle. Wind direction and speed based on ERA5 are indicated by the white arrow and text. (b) Overview of IME results. The title displays the satellite overpass time, source location, estimated emission rate, and associated uncertainty. Wind data from ERA5 and GEOS-FP are also shown. (c) Emission rates along individual CSF lines, shown in white in panel (b). The mean CSF emission rate and uncertainty are shown in the title.

https://doi.org/10.5194/egusphere-2025-6127
Preprint. Discussion started: 11 January 2026

3.1 Methane emissions

Figure 10 shows methane plumes from three sectors: oil & gas operations (Baku, Azerbaijan), coal mining (Shanxi, China), and solid waste management (Pirana landfill, Gujarat, India). Figure 10a–b presents multiple plumes captured in a single observation, while Fig. 10c–d shows plumes from the same landfill site detected by both EnMAP and PRISMA. All plumes follow the ERA5 wind directions, while the source locations are either near the facilities or the deposited waste. In the case of the second oil and gas plume, the plume is truncated due to the dark surface and shows a curved shape. This required manual adjustments to the plume detection settings, specifically increasing the azimuth difference threshold from 30° to 60°.

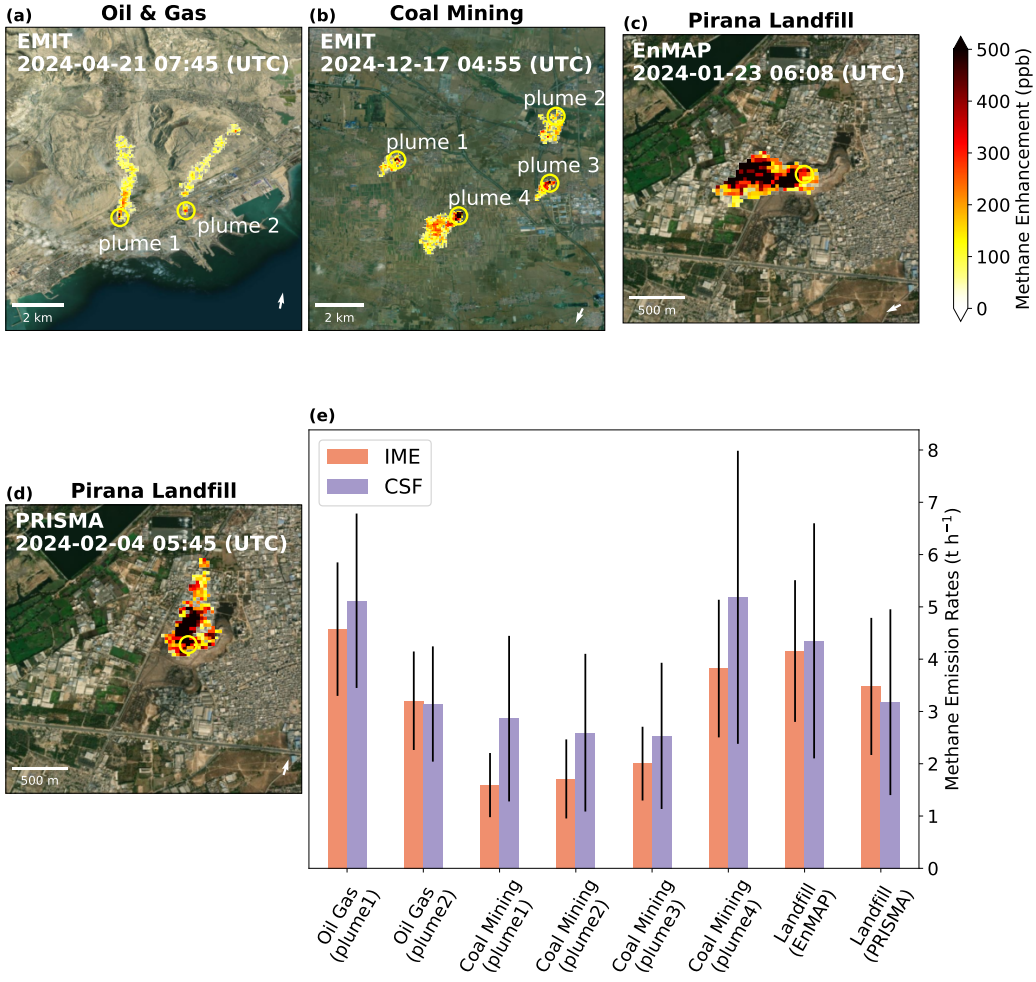

Figure 10. Methane plumes detected from various sectors using (a–b) EMIT, (c) EnMAP, and (d) PRISMA. Instrument and satellite overpass time are shown in white text at the top of each panel. Plume source locations are marked by yellow circles, with plume numbers annotated when multiple plumes are present in a single panel. ERA5 wind direction is indicated in the lower right corner of each image. (e) Methane emission estimates for the cases, derived using the IME and CSF methods. Background imagery source: Esri | Powered by Esri.

https://doi.org/10.5194/egusphere-2025-6127
Preprint. Discussion started: 11 January 2026

Figure 10e compares the IME and CSF estimates for the four cases. While the average CSF estimates tend to be higher, particularly for short plumes, both methods are consistent within their respective uncertainty ranges. The agreement between EnMAP and PRISMA measurements at the Pirana landfill indicates that multiple hyperspectral satellite datasets can be effectively integrated to analyze temporal patterns in landfill methane emissions, as previously described by Zhang et al. (2025). These findings highlight the potential for hyperspectral remote sensing to contribute to global methane monitoring and mitigation efforts.

3.2 Carbon dioxide emissions

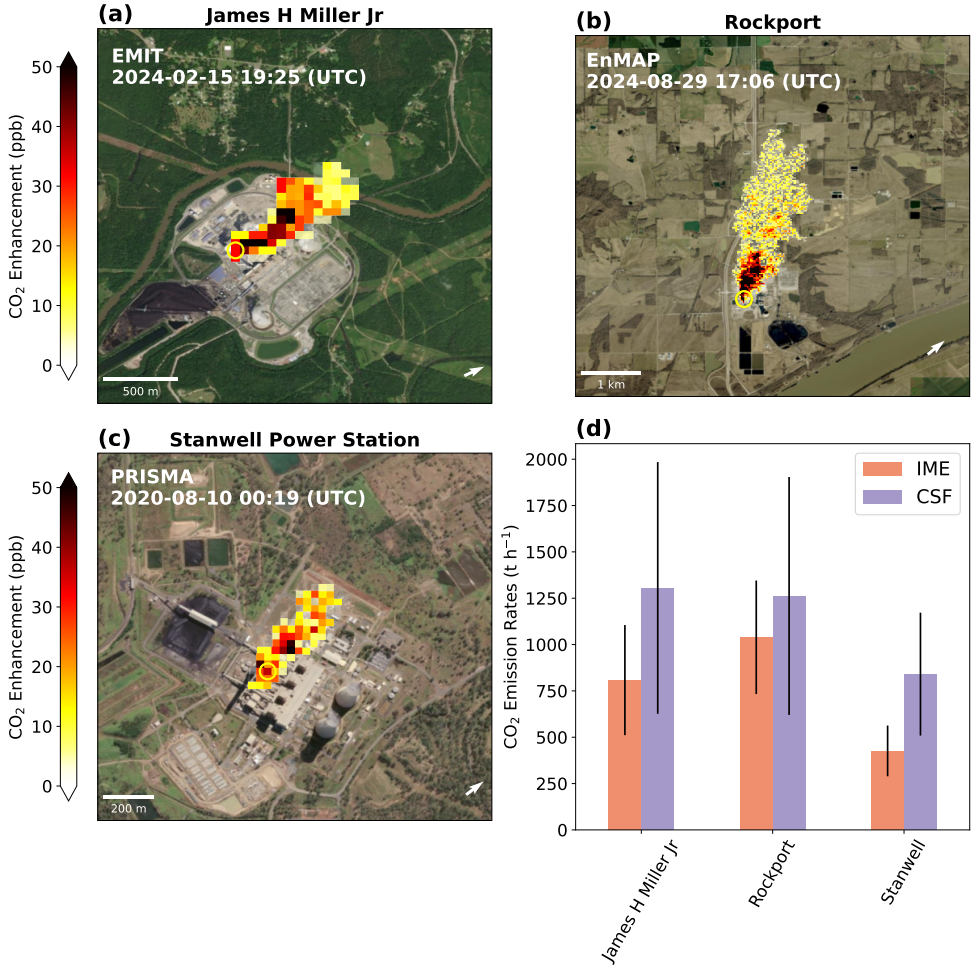

Figure 11. CO_2 plumes from power plants detected by (a) EMIT, (b) EnMAP, and (c) PRISMA. Instrument names and satellite overpass times are labeled in white text at the top of each panel. Yellow circles are identified plume source locations. Background ESRI imagery reproduced with permission as granted on Esri's website for noncommercial scholarly use Esri et al. (2022). (d) Emission rate estimates derived using the IME and CSF methods. Background imagery source: Esri | Powered by Esri.

https://doi.org/10.5194/egusphere-2025-6127
Preprint. Discussion started: 11 January 2026

In addition to methane, *HyperGas* also supports quantifying CO_2 emission rates. Figure 11a–c show CO_2 plumes from three power plants: James H. Miller Jr. (AL, USA), Rockport (IN, USA), and Stanwell Power Station (Stanwell, Australia). The estimated emission rates range from 0.5 to 2 kt h^{-1}. On average, CSF estimates tend to be higher, particularly for the compact plume observed at the Stanwell Power Station and James H. Miller Jr (Fig. 11d). This discrepancy may arise from plume simulations that assume surface-level sources and use only U_{10} to represent wind speed, whereas the actual CO_2 emissions are released as hot, buoyant plumes at heights greater than 10 m. Consequently, using U_{10} as a proxy may result in inaccurate wind speed calibrations for our observations, which could potentially affect emission estimates. Future refinements could involve CO_2-specific simulations to improve this calibration. Nevertheless, both IME and CSF estimates remain within their respective uncertainty bounds.

4 Conclusions

As hyperspectral satellite and airborne data become increasingly available, we have introduced the open-source package *HyperGas*, designed for retrieving atmospheric greenhouse gas enhancements, detecting, and quantifying greenhouse gas emissions. *HyperGas* provides modular tools and default settings to guide users through each stage of the analysis using an optimized and extendable workflow. We demonstrated how batch processing scripts and an interactive app enable both streamlined analysis and user-friendly interaction. For advanced users and developers, *HyperGas* offers the flexibility to implement custom algorithms at each step of the pipeline. This release enhances the standard matched filter retrieval by incorporating a lognormal matched filter and precise land/water masking. Users can further improve retrieval performance by applying their own pixel classification schemes and gas absorption coefficients, including aerosol scattering corrections (Feng et al., 2024).

We have also shown the integration of the open-source Python package *tobac*, originally developed for cloud tracking, to detect emission sources. Combined with a calibrated Chambolle total variation denoising (TV) filter, *HyperGas* generates plume masks that assist users in placing plume markers at source locations consistent with high-resolution visual imagery with the help of an interactive app.

For emission quantification, the package includes two established approaches, the integrated mass enhancement (IME) and the cross-sectional flux (CSF), along with default wind calibration settings. Users can assess uncertainties on the quantified emission rates, compare methods, and can modify the configuration for wind calibration routines. Further validation with additional methane controlled release experiments and hourly U.S. Environmental Protection Agency (EPA) CO_2 emission reports is recommended to determine the most appropriate method for various observational scenarios.

This initial release (*HypeGas* v1.0) provides robust functionality that can serve as the foundation for several additional features that can be developed in the future, including:

1. Automatic co-registration of PRISMA data (De Luca et al., 2024) to correct spatial misalignment between PRISMA imagery and actual Earth surface features.

https://doi.org/10.5194/egusphere-2025-6127
Preprint. Discussion started: 11 January 2026

2. Integration of the Weighting Function Modified Differential Optical Absorption Spectroscopy (WFM-DOAS; Krings et al., 2011; Thorpe et al., 2014; Borchardt et al., 2021) method for gas retrievals.
3. Extension to additional trace gases, such as nitrogen dioxide (NO_2; Borger et al., 2025).
4. Addition of additional plume quantification approaches, such as the linear integrate mass enhancement method (Hakkarainen et al., 2025).
5. Support for upcoming global hyperspectral missions, including the Copernicus Hyperspectral Imaging Mission for the Environment (CHIME; Rast et al., 2021) and the Surface Biology and Geology mission (SBG; Cawse-Nicholson et al., 2021).

The main goal of *HyperGas* is to build a consistent and transparent system for quantifying anthropogenic emissions using hyperspectral observations. We welcome community contributions to expand its capabilities and to establish *HyperGas* as a foundation for ongoing methodological and scientific advancements.

Code and data availability. The *HyperGas* source code is publicly available in a GitHub repository distributed under the Apache-2.0 license at https://github.com/SRON-ESG/HyperGas, and is archived and synchronized with Zenodo (https://doi.org/10.5281/zenodo.18154956; Zhang, 2026a). The latest version of *HyperGas* can be installed using conda with the command `conda install -c conda-forge hypergas`. Notebooks for reproducing this work, along with the associated input data, are deposited on Zenodo (https://doi.org/10.5281/zenodo.17854157 and https://doi.org/10.5281/zenodo.18162026; Zhang, 2026b, c). The ERA5 and GEOS-FP 10-m hourly wind data used in the analysis are also archived on Zenodo (https://doi.org/10.5281/zenodo.18166595; Zhang, 2026d). The original wind data products are provided by the Copernicus Climate Data Store (https://cds.climate.copernicus.eu/; Hersbach et al., 2023) and the Global Modeling and Assimilation Office (https://gmao.gsfc.nasa.gov/GMAO_products/; GMAO and NASA).

Appendix A: Comparisons between matched filter and clustered matched filter

Appendix B: *HyperGas* products

Author contributions. X.Z., J.D.M., and I.A. designed the research; X.Z. performed research with contributions from J.D.M.; X.Z. developed the package with contributions from T.A.d.J.; X.Z. analyzed the emission results with support from J.D.M.; P.T. assisted the forward model simulations; F.R., A.R.B., E.A.K, and T.J.A. organized and summarized the controlled release experiments; X.Z., J.D.M., and I.A. wrote the paper; and all authors discussed the results and commented on the manuscript.

Competing interests. The contact author has declared that none of the authors have any competing interests.

https://doi.org/10.5194/egusphere-2025-6127
Preprint. Discussion started: 11 January 2026

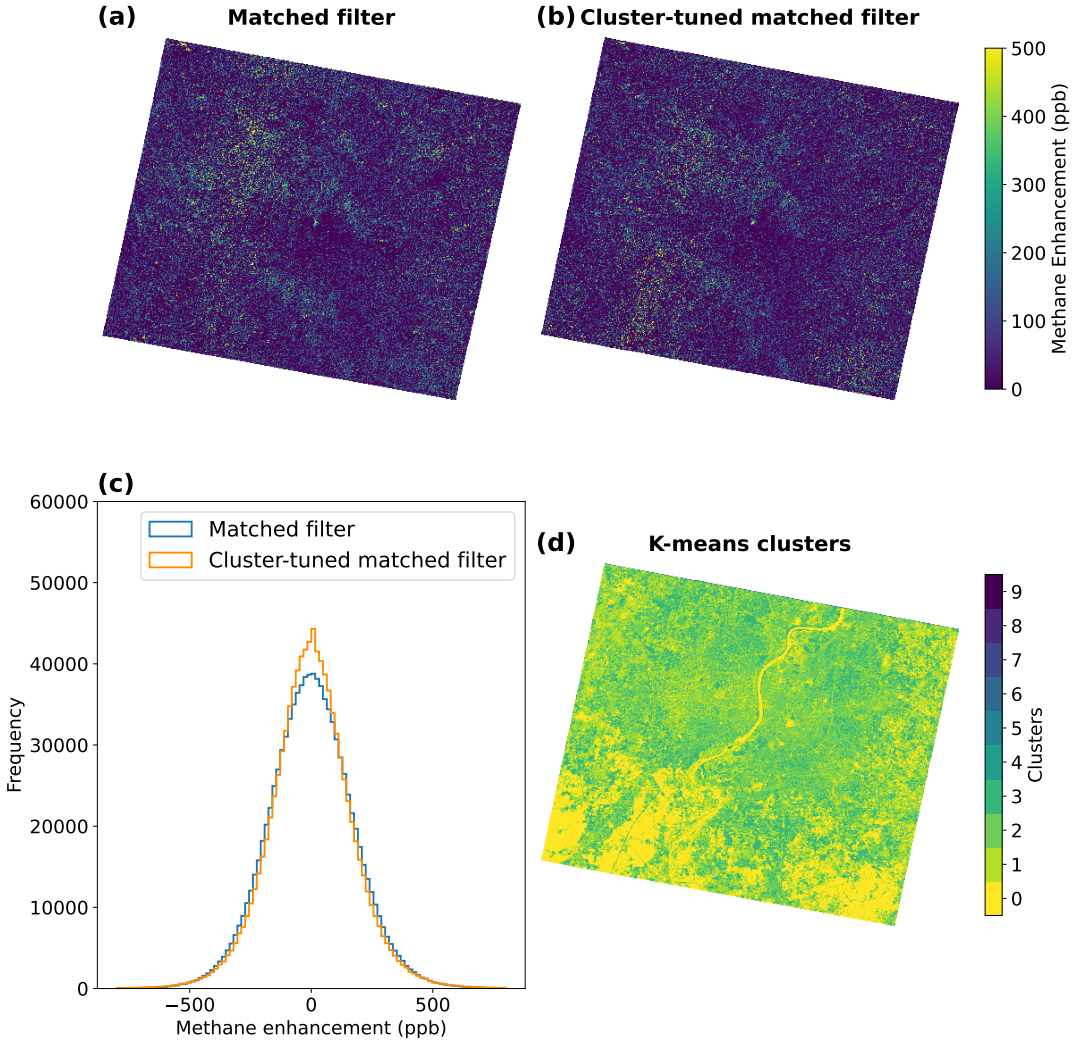

Figure A1. Retrieved methane enhancement using (a) the matched filter and (b) the cluster-tuned matched filter; (c) corresponding enhancement histograms; and (d) clusters applied in panel (b). The same scene is used in Fig. 10d.

Acknowledgements. This work was funded by the Targeting Waste emissions Observed from Space (TWOS) project funded by the Global Methane Hub. T.A.d J. acknowledges funding from the IMEO Science Studies programme contract DTIE22-EN5036. P.T. acknowledges funding from the NSO TROPOMI national program. We thank Daniel J. Varon for providing the WRF-LES simulations.

https://doi.org/10.5194/egusphere-2025-6127
Preprint. Discussion started: 11 January 2026

Table B1. *HyperGas* L2–L3 products table.

Product Level (format)	Name	Description
L2 (NetCDF)	ch4, co2	Retrieved gas enhancement using the base spectral windows (2110–2450 nm for methane and 1930–2200 nm for CO_2)
	ch4_comb, co2_comb	Retrieved gas enhancement using the full near-infrared spectral range (1300–2500 nm)
	ch4_denoise, co2_denoise	Denoised `ch4` and `co2` fields
	ch4_comb_denoise, co2_comb_denoise	Denoised `ch4_comb` and `co2_comb` fields
	ch4_mask, co2_mask	Automatically generated plume masks (0: background pixels; >0: plume pixels)
	radiance_2100	Top of the Atmosphere (TOA) radiance at 2100 nm, useful for assessing albedo effects
	rgb	RGB array for visualization
	segmentation	Water/land mask (0: ocean/lake; 1: land) or cluster map
	sp	Surface pressure
	u10	10-meter U-component wind from ERA5 and GEOS-FP
	v10	10-meter V-component wind from ERA5 and GEOS-FP
L3 (NetCDF)	ch4, co2, u10, v10, and sp	Subset of L2 variables restricted to plume pixels (as defined by the plume mask)

References

Batson, J. and Royer, L.: Noise2Self: Blind Denoising by Self-Supervision, in: Proceedings of the 36th International Conference on Machine Learning, pp. 524–533, PMLR, ISSN 2640-3498, 2019.

Borchardt, J., Gerilowski, K., Krautwurst, S., Bovensmann, H., Thorpe, A. K., Thompson, D. R., Frankenberg, C., Miller, C. E., Duren, R. M., and Burrows, J. P.: Detection and Quantification of CH_4 Plumes Using the WFM-DOAS Retrieval on AVIRIS-NG Hyperspectral Data, Atmospheric Measurement Techniques, 14, 1267–1291, https://doi.org/10.5194/amt-14-1267-2021, 2021.

Borger, C., Beirle, S., Butz, A., Scheidweiler, L. O., and Wagner, T.: High-Resolution Observations of NO_2 and CO_2 Emission Plumes from EnMAP Satellite Measurements, Environmental Research Letters, 20, 044 034, https://doi.org/10.1088/1748-9326/adc0b1, 2025.

CarbonMapper: Retrieved from https://data.carbonmapper.org, 2025.

https://doi.org/10.5194/egusphere-2025-6127
Preprint. Discussion started: 11 January 2026

Carver, R. W. and Merose, A.: ARCO-ERA5: An Analysis-Ready Cloud-Optimized Reanalysis Dataset, in: 103rd AMS Annual Meeting, AMS, 2023.

Cawse-Nicholson, K., Townsend, P. A., Schimel, D., Assiri, A. M., Blake, P. L., Buongiorno, M. F., Campbell, P., Carmon, N., Casey, K. A., Correa-Pabón, R. E., Dahlin, K. M., Dashti, H., Dennison, P. E., Dierssen, H., Erickson, A., Fisher, J. B., Frouin, R., Gatebe, C. K., Gholizadeh, H., Gierach, M., Glenn, N. F., Goodman, J. A., Griffith, D. M., Guild, L., Hakkenberg, C. R., Hochberg, E. J., Holmes, T. R. H., Hu, C., Hulley, G., Huemmrich, K. F., Kudela, R. M., Kokaly, R. F., Lee, C. M., Martin, R., Miller, C. E., Moses, W. J., Muller-Karger, F. E., Ortiz, J. D., Otis, D. B., Pahlevan, N., Painter, T. H., Pavlick, R., Poulter, B., Qi, Y., Realmuto, V. J., Roberts, D., Schaepman, M. E., Schneider, F. D., Schwandner, F. M., Serbin, S. P., Shiklomanov, A. N., Stavros, E. N., Thompson, D. R., Torres-Perez, J. L., Turpie, K. R., Tzortziou, M., Ustin, S., Yu, Q., Yusup, Y., and Zhang, Q.: NASA's Surface Biology and Geology Designated Observable: A Perspective on Surface Imaging Algorithms, Remote Sensing of Environment, 257, 112 349, https://doi.org/10.1016/j.rse.2021.112349, 2021.

Chambolle, A.: An Algorithm for Total Variation Minimization and Applications, Journal of Mathematical Imaging and Vision, 20, 89–97, https://doi.org/10.1023/B:JMIV.0000011325.36760.1e, 2004.

Cogliati, S., Sarti, F., Chiarantini, L., Cosi, M., Lorusso, R., Lopinto, E., Miglietta, F., Genesio, L., Guanter, L., Damm, A., Pérez-López, S., Scheffler, D., Tagliabue, G., Panigada, C., Rascher, U., Dowling, T. P. F., Giardino, C., and Colombo, R.: The PRISMA Imaging Spectroscopy Mission: Overview and First Performance Analysis, Remote Sensing of Environment, 262, 112 499, https://doi.org/10.1016/j.rse.2021.112499, 2021.

Cusworth, D. H., Thorpe, A. K., Miller, C. E., Ayasse, A. K., Jiorle, R., Duren, R. M., Nassar, R., Mastrogiacomo, J.-P., and Nelson, R. R.: Two Years of Satellite-Based Carbon Dioxide Emission Quantification at the World's Largest Coal-Fired Power Plants, Atmospheric Chemistry and Physics, 23, 14 577–14 591, https://doi.org/10.5194/acp-23-14577-2023, 2023.

De Luca, G., Carotenuto, F., Genesio, L., Pepe, M., Toscano, P., Boschetti, M., Miglietta, F., and Gioli, B.: Improving PRISMA Hyperspectral Spatial Resolution and Geolocation by Using Sentinel-2: Development and Test of an Operational Procedure in Urban and Rural Areas, ISPRS Journal of Photogrammetry and Remote Sensing, 215, 112–135, https://doi.org/10.1016/j.isprsjprs.2024.07.003, 2024.

Duren, R., Cusworth, D., Ayasse, A., Howell, K., Diamond, A., Scarpelli, T., Kim, J., O'neill, K., Lai-Norling, J., Thorpe, A., Zandbergen, S. R., Shaw, L., Keremedjiev, M., Guido, J., Giuliano, P., Goldstein, M., Nallapu, R., Barentsen, G., Thompson, D. R., Roth, K., Jensen, D., Eastwood, M., Reuland, F., Adams, T., Brandt, A., Kort, E. A., Mason, J., and Green, R. O.: The Carbon Mapper Emissions Monitoring System, EGUsphere, pp. 1–41, https://doi.org/10.5194/egusphere-2025-2275, 2025.

Duren, R. M., Thorpe, A. K., Foster, K. T., Rafiq, T., Hopkins, F. M., Yadav, V., Bue, B. D., Thompson, D. R., Conley, S., Colombi, N. K., Frankenberg, C., McCubbin, I. B., Eastwood, M. L., Falk, M., Herner, J. D., Croes, B. E., Green, R. O., and Miller, C. E.: California's Methane Super-Emitters, Nature, 575, 180–184, https://doi.org/10.1038/s41586-019-1720-3, 2019.

Esri, Maxar, Geographics, E., and the GIS User Community: ESRI World Imagery, https://services.arcgisonline.com/ArcGIS/rest/services/World_Imagery/ 2022.

Feng, C., Chen, S., Zeng, Z.-C., Luo, Y., Natraj, V., and Yung, Y. L.: Aerosol-Calibrated Matched Filter Method for Retrievals of Methane Point Source Emissions Over the Los Angeles Basin, Earth and Space Science, 11, e2024EA003 519, https://doi.org/10.1029/2024EA003519, 2024.

Foote, M. D., Dennison, P. E., Thorpe, A. K., Thompson, D. R., Jongaramrungruang, S., Frankenberg, C., and Joshi, S. C.: Fast and Accurate Retrieval of Methane Concentration From Imaging Spectrometer Data Using Sparsity Prior, IEEE Transactions on Geoscience and Remote Sensing, 58, 6480–6492, https://doi.org/10.1109/TGRS.2020.2976888, 2020.

https://doi.org/10.5194/egusphere-2025-6127
Preprint. Discussion started: 11 January 2026

Foote, M. D., Dennison, P. E., Sullivan, P. R., O'Neill, K. B., Thorpe, A. K., Thompson, D. R., Cusworth, D. H., Duren, R., and Joshi, S. C.: Impact of Scene-Specific Enhancement Spectra on Matched Filter Greenhouse Gas Retrievals from Imaging Spectroscopy, Remote Sensing of Environment, 264, 112 574, https://doi.org/10.1016/j.rse.2021.112574, 2021.

Funk, C., Theiler, J., Roberts, D., and Borel, C.: Clustering to Improve Matched Filter Detection of Weak Gas Plumes in Hyperspectral Thermal Imagery, IEEE Transactions on Geoscience and Remote Sensing, 39, 1410–1420, https://doi.org/10.1109/36.934073, 2001.

Gloudemans, A. M. S., Schrijver, H., Hasekamp, O. P., and Aben, I.: Error Analysis for CO and CH_4 Total Column Retrievals from SCIAMACHY 2.3 Mm Spectra, Atmospheric Chemistry and Physics, 8, 3999–4017, https://doi.org/10.5194/acp-8-3999-2008, 2008.

GMAO and NASA: GMAO Data Products.

Green, R. O., Mahowald, N., Ung, C., Thompson, D. R., Bator, L., Bennet, M., Bernas, M., Blackway, N., Bradley, C., Cha, J., Clark, P., Clark, R., Cloud, D., Diaz, E., Ben Dor, E., Duren, R., Eastwood, M., Ehlmann, B. L., Fuentes, L., Ginoux, P., Gross, J., He, Y., Kalashnikova, O., Kert, W., Keymeulen, D., Klimesh, M., Ku, D., Kwong-Fu, H., Liggett, E., Li, L., Lundeen, S., Makowski, M. D., Mazer, A., Miller, R., Mouroulis, P., Oaida, B., Okin, G. S., Ortega, A., Oyake, A., Nguyen, H., Pace, T., Painter, T. H., Pempejian, J., Garcia-Pando, C. P., Pham, T., Phillips, B., Pollock, R., Purcell, R., Realmuto, V., Schoolcraft, J., Sen, A., Shin, S., Shaw, L., Soriano, M., Swayze, G., Thingvold, E., Vaid, A., and Zan, J.: The Earth Surface Mineral Dust Source Investigation: An Earth Science Imaging Spectroscopy Mission, in: 2020 IEEE Aerospace Conference, pp. 1–15, ISSN 1095-323X, https://doi.org/10.1109/AERO47225.2020.9172731, 2020.

Green, R. O., Mahowald, N., Thompson, D. R., Ung, C., Brodrick, P., Pollock, R., Bennett, M., Lundeen, S., Joyce, M., Olson-Duvall, W., Oaida, B., Bradley, C., Diaz, E., Clark, R., Vannan, S., Swayze, G., Kokaly, R., Ginoux, P., Miller, R., Okin, G., Garcia-Pando, C. P., Ehlmann, B., Kalashnikova, O., Painter, T. H., Realmuto, V., Chadwick, D., Ben-Dor, E., Pearlshtien, D. H., Guanter, L., Phillips, B., Reath, K., Thorpe, A., Shaw, L., Keebler, A., Ochoa, F., Grant, K., Sen, A., Duren, R., Obiso, V., Gonçalves-Ageitos, M., and Huang, Y.: Performance and Early Results from the Earth Surface Mineral Dust Source Investigation (EMIT) Imaging Spectroscopy Mission, in: 2023 IEEE Aerospace Conference, pp. 1–10, ISSN 1095-323X, https://doi.org/10.1109/AERO55745.2023.10115851, 2023.

Guanter, L., Segl, K., Sang, B., Alonso, L., Kaufmann, H., and Moreno, J.: Scene-Based Spectral Calibration Assessment of High Spectral Resolution Imaging Spectrometers, Optics Express, 17, 11 594–11 606, https://doi.org/10.1364/OE.17.011594, 2009.

Guanter, L., Kaufmann, H., Segl, K., Foerster, S., Rogass, C., Chabrillat, S., Kuester, T., Hollstein, A., Rossner, G., Chlebek, C., Straif, C., Fischer, S., Schrader, S., Storch, T., Heiden, U., Mueller, A., Bachmann, M., Mühle, H., Müller, R., Habermeyer, M., Ohndorf, A., Hill, J., Buddenbaum, H., Hostert, P., Van der Linden, S., Leitão, P. J., Rabe, A., Doerffer, R., Krasemann, H., Xi, H., Mauser, W., Hank, T., Locherer, M., Rast, M., Staenz, K., and Sang, B.: The EnMAP Spaceborne Imaging Spectroscopy Mission for Earth Observation, Remote Sensing, 7, 8830–8857, https://doi.org/10.3390/rs70708830, 2015.

Guanter, L., Irakulis-Loitxate, I., Gorroño, J., Sánchez-García, E., Cusworth, D. H., Varon, D. J., Cogliati, S., and Colombo, R.: Mapping Methane Point Emissions with the PRISMA Spaceborne Imaging Spectrometer, Remote Sensing of Environment, 265, 112 671, https://doi.org/10.1016/j.rse.2021.112671, 2021.

Hakkarainen, J., Ialongo, I., Varon, D. J., Kuhlmann, G., and Krol, M. C.: Linear Integrated Mass Enhancement: A Method for Estimating Hotspot Emission Rates from Space-Based Plume Observations, Remote Sensing of Environment, 319, 114 623, https://doi.org/10.1016/j.rse.2025.114623, 2025.

Han, G., Pei, Z., Shi, T., Mao, H., Li, S., Mao, F., Ma, X., Zhang, X., and Gong, W.: Unveiling Unprecedented Methane Hotspots in China's Leading Coal Production Hub: A Satellite Mapping Revelation, Geophysical Research Letters, 51, e2024GL109 065, https://doi.org/10.1029/2024GL109065, 2024.

https://doi.org/10.5194/egusphere-2025-6127
Preprint. Discussion started: 11 January 2026

Heikenfeld, M., Marinescu, P. J., Christensen, M., Watson-Parris, D., Senf, F., van den Heever, S. C., and Stier, P.: Tobac 1.2: Towards a Flexible Framework for Tracking and Analysis of Clouds in Diverse Datasets, Geoscientific Model Development, 12, 4551–4570, https://doi.org/10.5194/gmd-12-4551-2019, 2019.

Hersbach, H., Bell, B., Berrisford, P., Hirahara, S., Horányi, A., Muñoz-Sabater, J., Nicolas, J., Peubey, C., Radu, R., Schepers, D., Simmons, A., Soci, C., Abdalla, S., Abellan, X., Balsamo, G., Bechtold, P., Biavati, G., Bidlot, J., Bonavita, M., Chiara, G., Dahlgren, P., Dee, D., Diamantakis, M., Dragani, R., Flemming, J., Forbes, R., Fuentes, M., Geer, A., Haimberger, L., Healy, S., Hogan, R. J., Hólm, E., Janisková, M., Keeley, S., Laloyaux, P., Lopez, P., Lupu, C., Radnoti, G., Rosnay, P., Rozum, I., Vamborg, F., Villaume, S., and Thépaut, J.-N.: The ERA5 Global Reanalysis, Quarterly Journal of the Royal Meteorological Society, 146, 1999–2049, https://doi.org/10.1002/qj.3803, 2020.

Hersbach, H., Bell, B., Berrisford, P., Biavati, G., Horányi, A., Muñoz Sabater, J., Nicolas, J., Peubey, C., Radu, R., Rozum, I., Schepers, D., Simmons, A., Soci, C., Dee, D., and Thépaut, J.-N.: ERA5 Hourly Data on Single Levels from 1940 to Present, https://doi.org/10.24381/cds.adbb2d47, 2023.

Hoyer, S. and Hamman, J. J.: Xarray: N-D Labeled Arrays and Datasets in Python, Journal of Open Research Software, 5, 10, https://doi.org/10.5334/jors.148, 2017.

Intergovernmental Panel on Climate Change (IPCC): Climate Change 2021 – The Physical Science Basis: Working Group I Contribution to the Sixth Assessment Report of the Intergovernmental Panel on Climate Change, Cambridge University Press, Cambridge, https://doi.org/10.1017/9781009157896, 2023.

Jacob, D. J., Varon, D. J., Cusworth, D. H., Dennison, P. E., Frankenberg, C., Gautam, R., Guanter, L., Kelley, J., McKeever, J., Ott, L. E., Poulter, B., Qu, Z., Thorpe, A. K., Worden, J. R., and Duren, R. M.: Quantifying Methane Emissions from the Global Scale down to Point Sources Using Satellite Observations of Atmospheric Methane, Atmospheric Chemistry and Physics, 22, 9617–9646, https://doi.org/10.5194/acp-22-9617-2022, 2022.

Kennedy, J. H., Smale, J., Johnston, A., Kristenson, H., Player, A., cirrusasf, Herrmann, J., Williams, F., Rine, J., and Logan, T.: ASFHyP3/Asf-Tools: ASF Tools v0.7.2, Zenodo, https://doi.org/10.5281/zenodo.10845708, 2024.

Krings, T., Gerilowski, K., Buchwitz, M., Reuter, M., Tretner, A., Erzinger, J., Heinze, D., Pflüger, U., Burrows, J. P., and Bovensmann, H.: MAMAP – a New Spectrometer System for Column-Averaged Methane and Carbon Dioxide Observations from Aircraft: Retrieval Algorithm and First Inversions for Point Source Emission Rates, Atmospheric Measurement Techniques, 4, 1735–1758, https://doi.org/10.5194/amt-4-1735-2011, 2011.

Kuhlmann, G., Koene, E., Meier, S., Santaren, D., Broquet, G., Chevallier, F., Hakkarainen, J., Nurmela, J., Amorós, L., Tamminen, J., and Brunner, D.: The *Ddeq* Python Library for Point Source Quantification from Remote Sensing Images (Version 1.0), Geoscientific Model Development, 17, 4773–4789, https://doi.org/10.5194/gmd-17-4773-2024, 2024.

Liu, Y.-N., Sun, D.-X., Hu, X.-N., Ye, X., Li, Y.-D., Liu, S.-F., Cao, K.-Q., Chai, M.-Y., Zhou, W.-Y.-N., Zhang, J., Zhang, Y., Sun, W.-W., and Jiao, L.-L.: The Advanced Hyperspectral Imager: Aboard China's GaoFen-5 Satellite, IEEE Geoscience and Remote Sensing Magazine, 7, 23–32, https://doi.org/10.1109/MGRS.2019.2927687, 2019.

Loizzo, R., Guarini, R., Longo, F., Scopa, T., Formaro, R., Facchinetti, C., and Varacalli, G.: Prisma: The Italian Hyperspectral Mission, in: IGARSS 2018 - 2018 IEEE International Geoscience and Remote Sensing Symposium, pp. 175–178, ISSN 2153-7003, https://doi.org/10.1109/IGARSS.2018.8518512, 2018.

Maasakkers, J. D., Varon, D. J., Elfarsdóttir, A., McKeever, J., Jervis, D., Mahapatra, G., Pandey, S., Lorente, A., Borsdorff, T., Foorthuis, L. R., Schuit, B. J., Tol, P., van Kempen, T. A., van Hees, R., and Aben, I.: Using Satellites to Uncover Large Methane Emissions from Landfills, Science Advances, 8, eabn9683, https://doi.org/10.1126/sciadv.abn9683, 2022.

https://doi.org/10.5194/egusphere-2025-6127
Preprint. Discussion started: 11 January 2026

Pearlman, J., Carman, S., Segal, C., Jarecke, P., Clancy, P., and Browne, W.: Overview of the Hyperion Imaging Spectrometer for the NASA EO-1 Mission, in: IGARSS 2001. Scanning the Present and Resolving the Future. Proceedings. IEEE 2001 International Geoscience and Remote Sensing Symposium (Cat. No.01CH37217), vol. 7, pp. 3036–3038 vol.7, https://doi.org/10.1109/IGARSS.2001.978246, 2001.

Pei, Z., Han, G., Mao, H., Chen, C., Shi, T., Yang, K., Ma, X., and Gong, W.: Improving Quantification of Methane Point Source Emissions from Imaging Spectroscopy, Remote Sensing of Environment, 295, 113 652, https://doi.org/10.1016/j.rse.2023.113652, 2023.

Qian, S.-E.: Hyperspectral Satellites, Evolution, and Development History, IEEE Journal of Selected Topics in Applied Earth Observations and Remote Sensing, 14, 7032–7056, https://doi.org/10.1109/JSTARS.2021.3090256, 2021.

Raspaud, M., Hoese, D., Lahtinen, P., Holl, G., Proud, S., Finkensieper, S., Meraner, A., Dybbroe, A., Strandgren, J., yukaribbba, Lahtinen, P., Feltz, J., BENR0, Joro, S., Zhang, X., de Buyl, P., Youva, Ghiggi, G., Roberts, W., Rasmussen, L. Ø., ClementLaplace, Samain, O., mherbertson, Zhu, Y., Méndez, J. H. B., Isotr0py, seenno, rdaruwala, and bkremmli: Pytroll/Satpy: Version 0.59.0 (2025/11/07), Zenodo, https://doi.org/10.5281/zenodo.17552484, 2025.

Rast, M., Nieke, J., Adams, J., Isola, C., and Gascon, F.: Copernicus Hyperspectral Imaging Mission for the Environment (Chime), in: 2021 IEEE International Geoscience and Remote Sensing Symposium IGARSS, pp. 108–111, ISSN 2153-7003, https://doi.org/10.1109/IGARSS47720.2021.9553319, 2021.

Reuland, F. and Brandt, A.: Large-Scale Controlled Methane Releases for Satellite-Based Detection and Emission Quantification of Point-Sources, Ph.D. thesis, 2025.

Reuland, F., Adams, T., Galvin, K., Kort, E. A., and Brandt, A. R.: Large-Scale Controlled Methane Releases for Satellite-Based Detection and Emission Quantification of Point-Sources, https://doi.org/10.25740/qh001qt3946, 2025.

Roger, J., Guanter, L., Gorroño, J., and Irakulis-Loitxate, I.: Exploiting the Entire Near-Infrared Spectral Range to Improve the Detection of Methane Plumes with High-Resolution Imaging Spectrometers, Atmospheric Measurement Techniques, 17, 1333–1346, https://doi.org/10.5194/amt-17-1333-2024, 2024.

Sadavarte, P., Pandey, S., Maasakkers, J. D., Lorente, A., Borsdorff, T., Denier van der Gon, H., Houweling, S., and Aben, I.: Methane Emissions from Superemitting Coal Mines in Australia Quantified Using TROPOMI Satellite Observations, Environmental Science & Technology, 55, 16 573–16 580, https://doi.org/10.1021/acs.est.1c03976, 2021.

Schaum, A.: A Uniformly Most Powerful Detector of Gas Plumes against a Cluttered Background, Remote Sensing of Environment, 260, 112 443, https://doi.org/10.1016/j.rse.2021.112443, 2021.

Sherwin, E. D., Rutherford, J. S., Chen, Y., Aminfard, S., Kort, E. A., Jackson, R. B., and Brandt, A. R.: Single-Blind Validation of Space-Based Point-Source Detection and Quantification of Onshore Methane Emissions, Scientific Reports, 13, 3836, https://doi.org/10.1038/s41598-023-30761-2, 2023.

Sherwin, E. D., El Abbadi, S. H., Burdeau, P. M., Zhang, Z., Chen, Z., Rutherford, J. S., Chen, Y., and Brandt, A. R.: Single-Blind Test of Nine Methane-Sensing Satellite Systems from Three Continents, Atmospheric Measurement Techniques, 17, 765–782, https://doi.org/10.5194/amt-17-765-2024, 2024.

Storch, T., Honold, H.-P., Chabrillat, S., Habermeyer, M., Tucker, P., Brell, M., Ohndorf, A., Wirth, K., Betz, M., Kuchler, M., Mühle, H., Carmona, E., Baur, S., Mücke, M., Löw, S., Schulze, D., Zimmermann, S., Lenzen, C., Wiesner, S., Aida, S., Kahle, R., Willburger, P., Hartung, S., Dietrich, D., Plesia, N., Tegler, M., Schork, K., Alonso, K., Marshall, D., Gerasch, B., Schwind, P., Pato, M., Schneider, M., de los Reyes, R., Langheinrich, M., Wenzel, J., Bachmann, M., Holzwarth, S., Pinnel, N., Guanter, L., Segl, K., Scheffler, D., Foerster, S., Bohn, N., Bracher, A., Soppa, M. A., Gascon, F., Green, R., Kokaly, R., Moreno, J., Ong, C., Sornig, M., Wernitz, R., Bagschik, K.,

https://doi.org/10.5194/egusphere-2025-6127
Preprint. Discussion started: 11 January 2026

Reintsema, D., La Porta, L., Schickling, A., and Fischer, S.: The EnMAP Imaging Spectroscopy Mission towards Operations, Remote Sensing of Environment, 294, 113 632, https://doi.org/10.1016/j.rse.2023.113632, 2023.

Thompson, D. R., Leifer, I., Bovensmann, H., Eastwood, M., Fladeland, M., Frankenberg, C., Gerilowski, K., Green, R. O., Kratwurst, S., Krings, T., Luna, B., and Thorpe, A. K.: Real-Time Remote Detection and Measurement for Airborne Imaging Spectroscopy: A Case Study with Methane, Atmospheric Measurement Techniques, 8, 4383–4397, https://doi.org/10.5194/amt-8-4383-2015, 2015.

Thorpe, A. K., Roberts, D. A., Bradley, E. S., Funk, C. C., Dennison, P. E., and Leifer, I.: High Resolution Mapping of Methane Emissions from Marine and Terrestrial Sources Using a Cluster-Tuned Matched Filter Technique and Imaging Spectrometry, Remote Sensing of Environment, 134, 305–318, https://doi.org/10.1016/j.rse.2013.03.018, 2013.

Thorpe, A. K., Frankenberg, C., and Roberts, D. A.: Retrieval Techniques for Airborne Imaging of Methane Concentrations Using High Spatial and Moderate Spectral Resolution: Application to AVIRIS, Atmospheric Measurement Techniques, 7, 491–506, https://doi.org/10.5194/amt-7-491-2014, 2014.

Thorpe, A. K., Green, R. O., Thompson, D. R., Brodrick, P. G., Chapman, J. W., Elder, C. D., Irakulis-Loitxate, I., Cusworth, D. H., Ayasse, A. K., Duren, R. M., Frankenberg, C., Guanter, L., Worden, J. R., Dennison, P. E., Roberts, D. A., Chadwick, K. D., Eastwood, M. L., Fahlen, J. E., and Miller, C. E.: Attribution of Individual Methane and Carbon Dioxide Emission Sources Using EMIT Observations from Space, Science Advances, 9, eadh2391, https://doi.org/10.1126/sciadv.adh2391, 2023.

Varon, D. J., Jacob, D. J., McKeever, J., Jervis, D., Durak, B. O. A., Xia, Y., and Huang, Y.: Quantifying Methane Point Sources from Fine-Scale Satellite Observations of Atmospheric Methane Plumes, Atmospheric Measurement Techniques, 11, 5673–5686, https://doi.org/10.5194/amt-11-5673-2018, 2018.

Varon, D. J., McKeever, J., Jervis, D., Maasakkers, J. D., Pandey, S., Houweling, S., Aben, I., Scarpelli, T., and Jacob, D. J.: Satellite Discovery of Anomalously Large Methane Point Sources From Oil/Gas Production, Geophysical Research Letters, 46, 13 507–13 516, https://doi.org/10.1029/2019GL083798, 2019.

Varon, D. J., Jacob, D. J., Jervis, D., and McKeever, J.: Quantifying Time-Averaged Methane Emissions from Individual Coal Mine Vents with GHGSat-D Satellite Observations, Environmental Science & Technology, 54, 10 246–10 253, https://doi.org/10.1021/acs.est.0c01213, 2020.

Zhang, X.: SRON-ESG/HyperGas: Version 0.3.5 (2026/01/05), Zenodo, https://doi.org/10.5281/zenodo.18154957, 2026a.

Zhang, X.: Dataset for "HyperGas1.0: A Python Package for Analyzing Hyperspectral Data for Greenhouse Gases from Retrieval to Emission Rate Quantification", https://doi.org/10.5281/zenodo.18162027, 2026b.

Zhang, X.: Zxdawn/HyperGas-GMD: Version 0.6 (2026/01/06), Zenodo, https://doi.org/10.5281/zenodo.18162804, 2026c.

Zhang, X.: Wind Dataset for "HyperGas1.0: A Python Package for Analyzing Hyperspectral Data for Greenhouse Gases from Retrieval to Emission Rate Quantification", https://doi.org/10.5281/zenodo.18166596, 2026d.

Zhang, X., van der A, R., Ding, J., Eskes, H., van Geffen, J., Yin, Y., Anema, J., Vagasky, C., L. Lapierre, J., and Kuang, X.: Spaceborne Observations of Lightning NO_2 in the Arctic, Environmental Science & Technology, 57, 2322–2332, https://doi.org/10.1021/acs.est.2c07988, 2023.

Zhang, X., Maasakkers, J. D., Roger, J., Guanter, L., Sharma, S., Lama, S., Tol, P., Varon, D. J., Cusworth, D. H., Howell, K., Thorpe, A. K., Brodrick, P. G., and Aben, I.: Global Identification of Solid Waste Methane Super Emitters Using Hyperspectral Satellites, Environmental Science & Technology, 59, 18 134–18 145, https://doi.org/10.1021/acs.est.4c14196, 2025.